Quantification of the Airborne Fraction of Atmospheric CO2 Reveals Stability in Global Carbon Sinks Over the Past Six Decades

Brian F. Bennett[1,2] , **Ross J. Salawitch[1,2,3]** , **Laura A. McBride[4]** , **Austin P. Hope[5]** , and **Walter R. Tribett[1]**

[1]Department of Atmospheric and Oceanic Science, University of Maryland-College Park, College Park, MD, USA, [2]Earth System Science Interdisciplinary Center, University of Maryland-College Park, College Park, MD, USA, [3]Department of Chemistry and Biochemistry, University of Maryland-College Park, College Park, MD, USA, [4]Department of Chemistry and Biochemistry, Albright College, Reading, PA, USA, [5]School of Marine and Atmospheric Sciences, Stony Brook University, Stony Brook, NY, USA

Abstract The airborne fraction of atmospheric CO_2 (AF), defined as the annual global CO_2 growth rate (dCO_2/dt) divided by the total emission of CO_2 from combustion of fossil fuels and land use change (LUC), has a long-term average of ~0.44 over the past six decades. When quantifying trends in AF it is important to account for inter-annual variability in dCO_2/dt due to natural factors such as the El Niño Southern Oscillation (ENSO) and major volcanic eruptions, as well as assumptions regarding LUC. Here, a multiple linear regression model is used to compute dCO_2/dt as a function of anthropogenic CO_2 emissions, ENSO indices, and stratospheric aerosol optical depth (a proxy for major volcanic eruptions), for numerous time series of the emission of CO_2 due to LUC (E_{LUC}). For 20 out of 21 previously published E_{LUC} time series, the trend in AF adjusted for natural variability (AF^{ADJ}) over 1959 to 2021 exhibits a trend that is statistically indistinguishable from zero and lacks statistical significance at the 95% confidence interval. Therefore, it is most likely that the relative efficacy of the combined global terrestrial biosphere and oceanic carbon sinks has been fairly constant on a global scale over the past six decades. Since the trend in AF exhibits considerable variability depending on which E_{LUC} time series is used, more precise knowledge of the actual value of the AF trend will require resolving the current large differences in various estimates of E_{LUC}.

Plain Language Summary The term airborne fraction (AF) refers to the annual rise in globally averaged atmospheric CO_2 divided by the total annual anthropogenic emissions of CO_2. There is considerable interest in determining whether AF is changing over time because a rise in AF would imply the existence of a feedback between climate change and the global carbon cycle. Such a feedback might inhibit society's ability to limit global warming to a particular threshold, such as the 1.5°C target and 2°C goal of the Paris Agreement. Here, we analyze trends in AF by accounting for variations in the annual growth rate of atmospheric CO_2 induced by ENSO events and major volcanic eruptions. We examine trends in AF over various time periods and for 21 previously published estimates of the global, annual emission of CO_2 due to land use change (E_{LUC}). For 20 out of these 21 estimates of E_{LUC}, we find that AF has not changed in a statistically significant manner over the past six decades. Our study also highlights the importance of resolving large differences in previously published estimates of E_{LUC} to better determine the true value of the trend in AF.

1. Introduction

It is well established that the increase in atmospheric carbon dioxide (CO_2) since the dawn of the Industrial Revolution, and perhaps as early as the Agricultural Revolution (Ruddiman et al., 2020), is nearly entirely due to human activity (IPCC, 2021). The rise in atmospheric CO_2 is the result of emissions from the combustion of fossil fuels, industrial processes, and cement production (E_{FOS}), as well as changes in land use (E_{LUC}) for agricultural and urban development (Friedlingstein et al., 2022). Just under half of all anthropogenic emissions of CO_2 have remained in the atmosphere throughout this time period (Canadell et al., 2021; van Marle et al., 2022). The annual global atmospheric CO_2 growth rate (i.e., the observed rise in the global CO_2 mixing ratio for a given year) has been subject to a high degree of interannual variability (IAV) over the past 60 years of continual-direct atmospheric CO_2 measurements (Ballantyne et al., 2012; Conway et al., 1994; Friedlingstein et al., 2022), despite a comparatively steady rise in annual anthropogenic emissions of CO_2. Much of the observed IAV comes from

Resources: Brian F. Bennett
Supervision: Ross J. Salawitch
Visualization: Brian F. Bennett
Writing – original draft: Brian F. Bennett
Writing – review & editing: Brian F. Bennett, Ross J. Salawitch, Laura A. McBride, Austin P. Hope, Walter R. Tribett

factors such as the El Niño Southern Oscillation (ENSO) (Betts et al., 2016; Gurney et al., 2012; Jones & Cox, 2005; Keeling et al., 1995; Zhang et al., 2019) and major volcanic eruptions that injected aerosol particles into the stratosphere, thereby altering the ratio of diffuse to direct sunlight (Dutton & Bodhaine, 2001; Dutton & Christy, 1992; Frölicher et al., 2013; Gu et al., 2003; Gurney et al., 2012) received at the surface. It has also long been recognized that feedbacks between climate change and the global carbon cycle due to factors such as drought (Cox et al., 2000; Zhao & Running, 2010), expansion or contraction of climatic regimes (Graham et al., 1990), the greening of the biosphere (Friedlingstein et al., 1995), and a possible decline in the global ocean sink efficiency (Revelle & Suess, 1957) can affect the uptake of CO_2 by both the ocean and land carbon sinks (Forkel et al., 2016; Grossiord et al., 2020; Pugh et al., 2018; Smith & Dukes, 2017). However, ocean uptake of CO_2 also depends on the strength of the overturning circulation, which varies on decadal time scales (DeVries et al., 2017). As such, the past and future evolution of the rise in atmospheric CO_2 depends on a considerable number of complex, interacting factors.

The annual Global Carbon Budget (GCB) 2022 report (Friedlingstein et al., 2022) defines the CO_2 mass balance as:

$$E_{FOS}(t) + E_{LUC}(t) = G_{ATM}(t) + S_{OCEAN}(t) + S_{LAND}(t) \qquad (1)$$

where the anthropogenic emissions of CO_2 due to fossil fuel combustion, industrial processes, and cement production, and land use change are represented on the left-hand side of Equation 1. The GCB 2022 estimate for E_{FOS} is based primarily upon energy data from the United Nations. In contrast, the estimate for E_{LUC} is based on output from several land use bookkeeping models in addition to multiple Dynamical Global Vegetation Models (DGVMs). The first term on the right side, G_{ATM}, is the annual mean global CO_2 growth rate in the atmosphere, referred to below as dCO_2/dt. The next two terms represent the carbon sinks, where the uptake of CO_2 by the oceans (S_{OCEAN}) is estimated using an ensemble of global ocean biochemistry models (GOBMs), where some models are constrained by ocean pCO_2 measurements (Fay et al., 2021), and the uptake of CO_2 by the land sinks (S_{LAND}) is estimated by multiple DGVMs. The terms in Equation 1 are typically evaluated in the GCB reports on an annual time scale.

The annual airborne fraction (AF) is the ratio of CO_2 that remains in the atmosphere relative to the total anthropogenic emission of CO_2 released over the course of a year:

$$AF(t) = \frac{dCO_2/dt\,(t)}{(E_{FOS}(t) + E_{LUC}(t))} \qquad (2)$$

AF is a simple metric used to examine the relative efficiency of the combined ocean and land carbon sinks. Numerous studies have investigated the trends in AF that have reached varied and often contradictory conclusions. Analyses by Canadell et al. (2007), Le Quéré et al. (2009), and Raupach et al. (2008, 2014) found that the trend in AF is positive, with statistical significance, when using filtering methods to remove the effects of natural variability from ENSO and volcanoes. Studies conducted by Knorr (2009) and Frölicher et al. (2013) reported that the trend in AF is negative, at a statistically insignificant level, when also accounting for natural variability from these factors. Ballantyne et al. (2012, 2015) and Bennedsen et al. (2019) found the trend in AF to be positive, although not statistically significant, without consideration for the influence of ENSO and major volcanic eruptions. A recent analysis conducted by van Marle et al. (2022) found that the trend in AF, when adjusted for ENSO and volcanoes, varies upon consideration of alternate E_{LUC} time series and report a decline in AF based on their independently estimated E_{LUC} data set. van Marle et al. (2022) calculate their E_{LUC} time series for use in their AF trend analysis from visibility observations used as a proxy for fire emissions, along with bookkeeping estimates for other regions of the terrestrial biosphere.

Earth System Models (ESMs) with coupled carbon cycles are becoming more prevalent when projecting global warming. Section 5.4.5 of the Intergovernmental Panel on Climate Change (IPCC) Sixth Assessment Report (AR6) (Canadell et al., 2021) details the response of atmospheric CO_2 for simulations conducted using ESMs with interactive carbon cycles. Canadell et al. (2021) conclude in Section 5.4.5.4 that "oceanic and terrestrial carbon sinks are projected to continue to grow with increasing atmospheric concentrations of CO_2, but the fraction of emissions taken up by land and ocean is expected to decline as the CO_2 concentration increases (high confidence)." In other words, the consensus of Canadell et al. (2021) is that AF will increase over time. If AF is indeed

increasing over time, then achieving the goal of the Paris Climate Agreement to limit the rise in global mean surface temperature to 1.5°C, with an upper limit of 2°C warming, would be considerably more challenging than is commonly appreciated (M. T. Huang & Zhai, 2021; Nicholls et al., 2021). Conversely, Pressburger et al. (2023) use a reduced complexity climate model with a representation of terrestrial and ocean carbon sinks in a Monte Carlo framework to conclude the trend in AF over 1960 to 2020 is highly likely to be negative.

In this study we conduct a trend analysis of AF over the observational period of 1959 through the end of 2021 using a value for AF found from the atmospheric growth rate of CO_2 ($AF^{GLB-RAW}$), as well as using a time series of AF adjusted for natural variability due to ENSO and stratospheric volcanic aerosols ($AF^{GLB-ADJ}$). We use the coefficients determined from a multiple linear regression (MLR) of dCO_2/dt as a function of the anthropogenic emission of CO_2, ENSO, and stratospheric aerosol optical depth (SAOD) over land as a proxy for volcanic activity to adjust the atmospheric CO_2 growth rate for these two natural influences. Unique to this MLR analysis is our treatment of ENSO separated into El Niño, neutral, and La Niña phases, an investigation of the combined effects of a Central Pacific (CP) and Eastern Pacific (EP) ENSO (N4 and N1+2, respectively) compared to a single ENSO index (N3.4) and our calculation of SAOD over land. Our primary time series for SOAD is based on two sources: extinction coefficients used by the Coupled Model Intercomparison Project Phase 6 (CMIP6) for Global Climate Models (GCMs) (Arfeuille et al., 2014), and the Global Space-based Stratospheric Aerosol Climatology (GloSSAC v2.2) (Thomason et al., 2018). Additionally, we quantify the sensitivity of trends in AF to other specifications of SAOD. We assess the statistical significance of trends in AF using a series of Monte Carlo (MC) simulations, in which the full range of uncertainty in each component of AF is considered. Furthermore, we investigate the sensitivity of the trends in AF to variations in start and end year. We repeat this analysis both with 20 alternate data sets for E_{LUC} from various modeling methods and one without E_{LUC} to calculate AF trends determined from E_{FOS} only. A description of the data used, the MLR model, and the MC analysis appear in Section 2. Section 3 details our results from these experiments, a discussion is provided in Section 4, and concluding remarks are in Section 5.

2. Data and Methodology

2.1. Model Inputs

2.1.1. Atmospheric CO_2 Growth Rate

Here we describe the computation of the atmospheric CO_2 growth rate. The National Oceanic and Atmospheric Administration's (NOAA) Earth System Research Laboratories (ESRL) defines the annual mean global CO_2 growth rate (herein referred to as $dCO_2^{GLB-RAW}/dt$) as the difference between globally averaged deseasonalized mixing ratio of CO_2, from the end of the year relative to the beginning of the year. The global atmospheric CO_2 mixing ratios used to compute the annual CO_2 growth rate are the averages of the December and January monthly values: that is, the average of monthly mean CO_2 measured in December 2019 and January 2020 is used to define CO_2 at the end of 2019 and at the beginning of 2020. The time series of $dCO_2^{GLB-RAW}/dt$, provided by NOAA ESRL, is shown in Figure 1b as the gray line, with dark and light shading representing the $\pm 1\sigma$ and $\pm 2\sigma$ total uncertainties of this quantity as provided by NOAA (Ballantyne et al., 2012; Conway et al., 1994).

We compute $dCO_2^{GLB-RAW}/dt$ at a monthly time resolution (blue line in Figure 1b) by taking the sliding difference of the 2-month running mean of the deseasonalized atmospheric global monthly mean CO_2 mixing ratio (orange line in Figure 1a) between successive years from 1980 onward, that is,:

$$dCO_2^{GLB\text{-}RAW}/dt\,(t) = \frac{CO_2(t-0.5) + CO_2(t+0.5)}{2} - \frac{CO_2(t-11.5) + CO_2(t-12.5)}{2} \qquad (3)$$

In Equation 3 the increment of t is 1 month: the use of 2-month means is motivated by our desire to be consistent with formalism adopted by NOAA ESRL for their computation of the annual growth rate. A global time series of monthly atmospheric CO_2 is not available before 1979. Similar to Raupach et al. (2008, 2014) and Ballantyne et al. (2012, 2015), we have reconstructed an estimate for global monthly mean CO_2 from 1959 onward by taking the average of observations of CO_2 at Mauna Loa, Hawaii (MLO) and the South Pole (SPO), provided by NOAA ESRL and the Scripps Institution of Oceanography (light blue line in Figure 1a). We again take the sliding difference between subsequent years of the 2-month running mean of the deseasonalized CO_2 monthly mean at MLO and SPO from the beginning of 1959 through 1980 to expand $dCO_2^{GLB-RAW}/dt$ to a monthly time grid. The
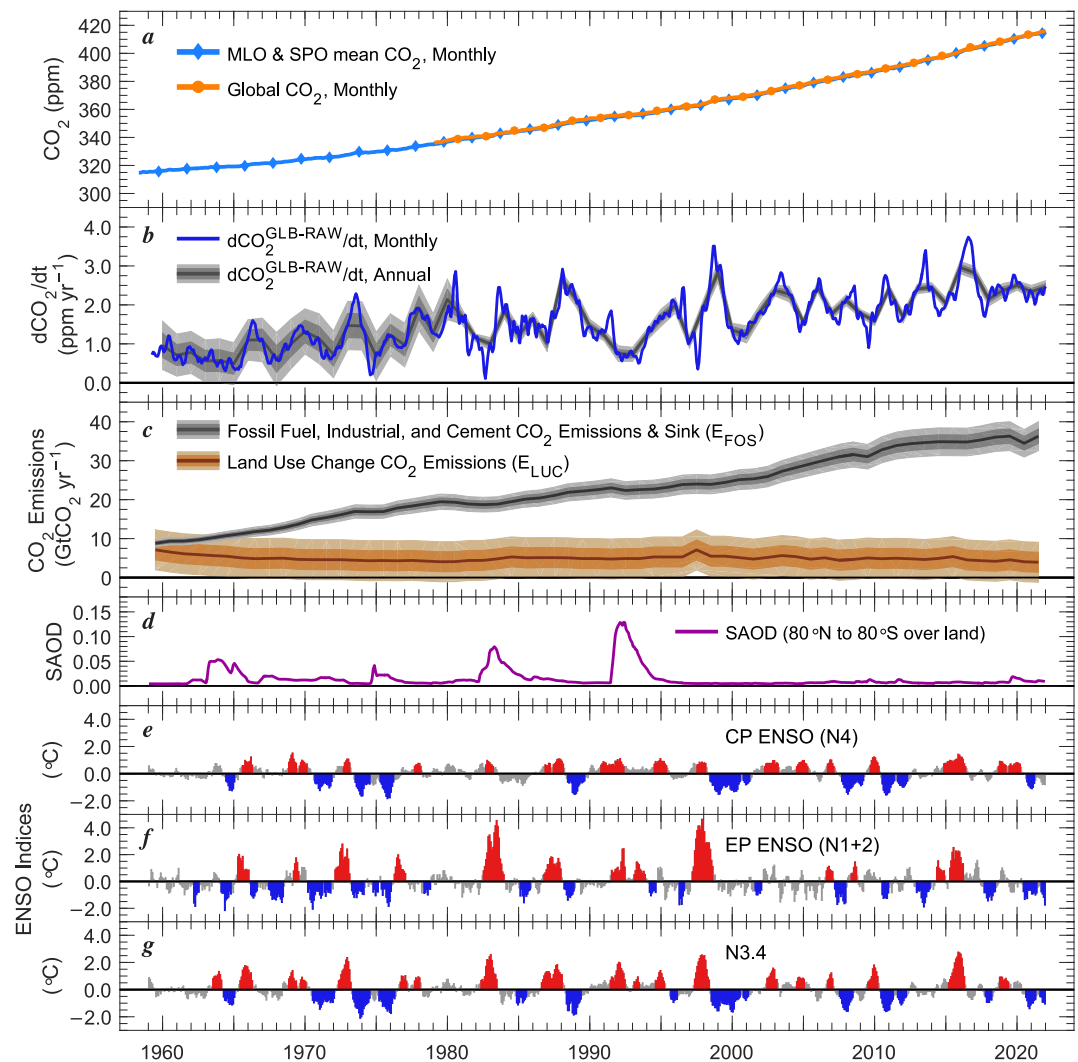
Figure 1. Time series used to model the annual growth rate of atmospheric CO_2. (a) Seasonally adjusted 2-month running mean of globally averaged CO_2 mixing ratios (orange), beginning of 1979 through the end of 2021, and seasonally adjusted 2-month running mean of the average of the CO_2 mixing ratio at Mauna Loa, HI (MLO) and the South Pole (SPO) (blue), beginning of 1959 through the end of 2021. NOAA ESRL provides global and MLO observations of CO_2; the Scripps Institution of Oceanography provides SPO observations of CO_2. (b) The annual atmospheric CO_2 growth rate ($dCO_2^{GLB-RAW}/dt$) at a monthly time step (blue) and annual time step with $\pm 1\sigma$ and $\pm 2\sigma$ total uncertainties (gray). $dCO_2^{GLB-RAW}/dt$ at an annual time step and the associated uncertainties are both provided by NOAA ESRL. $dCO_2^{GLB-RAW}/dt$ at monthly time steps is calculated from the seasonally adjusted CO_2 observations shown in (a) using Equation 3. (c) Anthropogenic CO_2 emissions from fossil fuel combustion, industrial processes, and cement production (E_{FOS}), including the cement carbonation sink, with $\pm 1\sigma$ and $\pm 2\sigma$ total uncertainties (gray) and from land use change (E_{LUC}), with $\pm 1\sigma$ and $\pm 2\sigma$ "semi-quantitative" uncertainties (brown) from GCB 2022 (Friedlingstein et al., 2022) (see Friedlingstein et al. for their definition of "semi-quantitative"). (d) Globally averaged stratospheric aerosol optical depth (SAOD) over land, used as a proxy for the influence of major volcanic eruptions, 80°N to 80°S, calculated from extinction coefficients used by CMIP6 GCMs for 1959 through 1978 and from SAOD in GloSSAC v2.2 from 1979 through the end of 2021. (e) Detrended Niño 4 index with El Niño, neutral, and La Niña phases in red, gray, and blue, respectively. (f) Detrended Niño 1+2 index with El Niño, neutral, and La Niña phases also in red, gray, and blue. (g) Detrended Niño 3.4 index with El Niño, neutral, and La Niña phases in red, gray, and blue. Phases of ENSO are classified by temperature anomalies above 0.5°C or below −0.5°C for 5 consecutive months.

last data point for $dCO_2^{GLB-RAW}/dt$ during the MLO and SPO time period occurs at 1980.083 with a value of 1.98 ± 0.10 ppm yr^{-1}, and the first data point for the global $dCO_2^{GLB-RAW}/dt$ calculated from global monthly CO_2 provided by NOAA occurs at 1980.125 with a value of 1.84 ± 0.10 ppm yr^{-1}. The similarity between the two

estimates of $dCO_2^{GLB-RAW}/dt$ shown in Figure 1b demonstrates that there is good continuity when joining these two time series, as is also visually apparent in Figures 1a and 1b.

The estimated uncertainty in the atmospheric CO_2 growth rate provided by NOAA (Figure 1b gray shading) decreases over the observational period due to the addition of numerous CO_2 monitoring sites around the world. The 1σ uncertainty of $dCO_2^{GLB-RAW}/dt$ is relatively high from 1959 to 1979, averaging about 32% of the reported growth rate over this time. The estimated uncertainty in the CO_2 growth rate is relatively high early in the record because this quantity is based only on observations made at MLO and SPO (Ballantyne et al., 2012). The calculated uncertainty is lower from 1980 onward, averaging about 5% of the reported growth rate. The more precise knowledge of the CO_2 growth rate is due to the addition of multiple air sampling observational sites worldwide (Conway et al., 1994).

We also analyze the CO_2 growth rate observed only at MLO in additional MLR modeling cases and in our AF trend analysis. We use data from this single site to address any potential issues that may result from reconstructing monthly $dCO_2^{GLB-RAW}/dt$ that combines data from MLO and SPO with the global data for different time periods. Furthermore, the uncertainty in dCO_2/dt at MLO ($dCO_2^{MLO-RAW}/dt$) is consistent at ± 0.11 ppm yr^{-1} for each year and comparatively lower than the uncertainty of $dCO_2^{GLB-RAW}/dt$. The annual mean carbon dioxide growth rate at MLO is defined by NOAA ESRL, again, as the difference between CO_2 mixing ratios observed at the end of the year and the beginning of the year. However, for MLO, the end and beginning of the year values of CO_2 are defined as the average of the November through February monthly mean observations of CO_2. As previously stated, the average December and January monthly values represent the end and beginning of the year for $dCO_2^{GLB-RAW}/dt$. A 4-month mean is used for the growth rate at MLO to limit the influence of month-to-month variability in the CO_2 mixing ratio that may arise from anomalous winds and weather patterns at this location. We use the 4-month running mean of deseasonalized CO_2 mixing ratios observed at MLO to calculate $dCO_2^{MLO-RAW}/dt$ at a monthly time resolution, by taking the sliding difference between subsequent years in a manner similar to Equation 3.

2.1.2. Anthropogenic CO_2 Emissions

Annual anthropogenic emissions of CO_2 due to fossil fuel combustion, industrial processes, and cement production (E_{FOS}), as well as emissions of CO_2 associated with land use change (E_{LUC}) are provided by GCB 2022 (Friedlingstein et al., 2022). The quantity E_{FOS}, shown by the black line in Figure 1c, is the annual summation of global emissions from the combustion of coal, natural gas, and liquid fuels. The quantity E_{FOS} includes CO_2 emissions from gas flaring, cement production, international aviation and maritime transport, as well as various other industrial processes. The GCB estimate of E_{FOS} is primarily based upon United Nations energy data. The report lists a $\pm 1\sigma$ total uncertainty for E_{FOS} as $\pm 5\%$ of annual emissions, shown by the gray shading in Figure 1c.

New to the GCB 2020 report was the inclusion of a term for the cement carbonation sink (Friedlingstein et al., 2020), which represents the absorption of atmospheric CO_2 by cement following its production. The GCB estimates the cement carbonation sink by taking the average from two studies (Cao et al., 2020; Guo et al., 2021) that utilize the same model (Xi et al., 2016) with different inputs and parametrizations. The GCB report does not include an uncertainty for this term. The cement carbonation sink is relatively small, removing an average of 2.1% of E_{FOS} from the atmosphere over the past decade. We assume this term is perfectly known because the magnitude of this sink is less than the 1σ total uncertainty of E_{FOS}.

The quantity E_{LUC} accounts for CO_2 fluxes from deforestation, afforestation, logging, shifting cultivation, regrowth of forests, and some land management activities (Friedlingstein et al., 2022), as shown by the brown line in Figure 1c. The GCB estimates E_{LUC} by taking the average of three bookkeeping models: H&N (Houghton & Nassikas, 2017), BLUE (bookkeeping of land use emissions) (Hansis et al., 2015), and OSCAR (Gasser et al., 2020). The report lists a $\pm 1\sigma$ semi-quantitative uncertainty for E_{LUC} as 0.7 GtC yr^{-1} (± 2.57 GtCO$_2$ yr^{-1}) for each year, shown by the dark brown shading in Figure 1c.

We use the average of the three bookkeeping models for E_{LUC} in our baseline MLR and AF trend analysis. The GCB 2022 has also compiled 16 additional time series of E_{LUC} from various Dynamic Global Vegetative Models (DGVMs). We repeat our analysis using the three bookkeeping model estimates of E_{LUC} individually, the 16 alternate time series for E_{LUC} from each DGVM, and the mean of the 16 DGVMs. There are a total of 21 E_{LUC} estimates used in our analysis, all of which appear in Figure S1 in Supporting Information S1. We attribute an

uncertainty of ± 2.05 $GtCO_2$ yr^{-1} to the 16 DGVMs, calculated as the mean of the annual standard deviation across the 16 DGVMs. Annual CO_2 emissions for all terms are assumed to represent emissions at the midpoint of each year and are linearly interpolated onto a monthly time step for use in our MLR model in order to adjust the CO_2 growth rate for the influence of major volcanic eruptions and ENSO.

2.1.3. Stratospheric Aerosol Optical Depth

Major volcanic eruptions that inject large amounts of SO_2 into the stratosphere have the potential to increase the global uptake of atmospheric CO_2 by plant photosynthesis, as explained below. In the stratosphere, volcanically injected SO_2 is converted to H_2SO_4 (sulfate aerosols), thereby enhancing stratospheric aerosol optical depth (SAOD). The light scattering properties of sulfate aerosols in the stratosphere following major volcanic eruptions lead to substantial increases in the amount of diffuse solar irradiance reaching the surface, as well as significant decreases in the amount of direct solar radiation at the surface (Dutton & Bodhaine, 2001; Dutton & Christy, 1992). Diffuse irradiance observed at MLO following the eruptions of El Chichón and Mount Pinatubo increased by over 100 Wm^{-2}, and direct radiation decreased by approximately 100 Wm^{-2}, resulting in a net effect of a slight decline in total solar radiation by about -7 $W\,m^{-2}$ (E. G. Dutton & Bodhaine, 2001). Since scattered light (diffuse irradiance) penetrates deeper into canopies than direct radiation, photosynthesis by the world's forests increases during times of enhanced SAOD, resulting in a drawn-down of atmospheric CO_2. An observed increase in photosynthesis occurred at Harvard Forest (a deciduous forest at 42.5°N, 72.2°W) following the eruption of Mount Pinatubo (Gu et al., 2003), attributed to an enhancement in diffuse irradiance. Additionally, some studies have attributed the observed drawdown in CO_2 following the eruption of Mt. Pinatubo to reduced plant respiration resulting from decreases in surface temperature (Jones & Cox, 2001; Lucht et al., 2002).

We calculate a time series for SAOD over global land surfaces from 1959 through the end of 2021 (purple line in Figure 1d) from two sources for use in the MLR analysis. From 1959 to the end of 1978, SAOD is calculated from extinction coefficients at 550 nm from the volcanic forcing data set used in CMIP6 GCMs (Arfeuille et al., 2014). The extinction coefficients, provided as a function of latitude and altitude, are integrated from the tropopause to an altitude of 39.5 km, at each 5° latitude bin from 80°S to 80°N. For the time period of 1979 through the end of 2020, SAOD values from the Global Space-based Stratospheric Aerosol Climatology (GloSSAC v2.2) (Thomason et al., 2018) data set at 525 nm in 5° latitude bins are used to calculate global SAOD from 80°S to 80°N.

The influence of SAOD on the carbon cycle occurs primarily over the terrestrial biosphere. Therefore, SAOD is weighted by the land fraction at each latitude using the NOAA GHCN_CAMS Gridded 2m Temperature (Land) data set (Fan & van den Dool, 2008). To approximate global mean SAOD over land, monthly mean SAOD is weighted by the product of cosine latitude (surrogate for area) times the land fraction at each latitude. Figure S2 in Supporting Information S1 shows the comparison of global mean SAOD weighted by cosine latitude alone and weighted by both the product of cosine latitude and the land fraction. The greatest difference between these two SAOD time series occurs after the 1963 eruption of Mount Agung in Indonesia. This eruption had a much more considerable influence on SAOD in the southern hemisphere than the northern hemisphere, resulting in a reduction of SAOD upon using the land fraction term. A moderate enhancement in SAOD due to land fraction weighting occurs after the 1982 eruption of El Chichón in Mexico. Little effect is seen following the eruptions of Fuego in 1974 and Mount Pinatubo in 1991. Throughout our analysis, we refer to this single time series of global SAOD over land combined from two data sources as the CMIP6-GloSSAC record.

Numerous prior studies have quantified the trend in AF based on a time series for the CO_2 growth rate adjusted for ENSO and volcanoes (Canadell et al., 2007; Knorr, 2009; Le Quéré et al., 2009; Raupach et al., 2008, 2014; van Marle et al., 2022). The time series for SAOD used in nearly all the prior studies was based upon the Volcanic Aerosol Index (VAI) of Ammann et al. (2003a, 2003b). The VAI provides SAOD at 2.8° latitude bins from 1890 through 1999. Figure S2 in Supporting Information S1 also shows the global SAOD we calculate from the VAI, weighted by the cosine of latitude, from 1959 through 1999, as well as the SAOD record of Sato et al. (1993).

The VAI time series differs from the CMIP6-GloSSAC record we calculate in three distinct ways (Figure S2 in Supporting Information S1). First, the VAI time series of Ammann et al. (2003a, 2003b) shows greater increases in SAOD following the eruptions of Mount Agung, El Chichón, and Mount Pinatubo compared to the CMIP6-GloSSAC data record. Second, SAOD approaches zero during time periods where there is no volcanic activity in the VAI record, whereas the minimum value of SAOD in the CMIP6-GloSSAC records is substantially larger than zero. Third, there is a pronounced increase in SAOD in 1968 attributed to the eruption of Fernandina in the

Galapagos Islands (0S 92W) within the VAI record that is not present in the CMIP6 volcanic forcing data record. The record of Sato et al. (1993) shows a moderate enhancement in SAOD compared to the CMIP6-GloSSAC data record for El Chichón, and Mount Pinatubo, but not Mount Agung. The eruption of Fernandina also appears in the Sato et al. (1993) SAOD record.

Ammann et al. (2003a, 2003b) base their estimate of SAOD for the time period of the Fernandina eruption on the reduction of direct solar radiation from data by Dyer and Hicks (1968). Ammann et al. (2003a, 2003b) note that Dyer and Hicks (1968) questioned the accuracy of this data during the 1960 to 1978 time period, which also includes the eruption of Mount Agung. Sato et al. (1993) estimate SAOD for the time period of the Fernandina eruption based on variations in optical depth determined from the brightness of sunlight refracted and scattered into Earth's geometrical shadow during total lunar eclipses, from data by Keen (1983). Arfeuille et al. (2014) provide a volcanic forcing data set for climate modeling, which for the time of the Fernandina eruption is based upon sulfate depositions in Greenland and Antarctica present in the ice core record of Gao et al. (2008). It is unclear why the stratospheric impact of the Fernandina eruption is apparent in the direct solar radiation and lunar eclipse data but not in the ice core record. We append the VAI through the end of 2021 with an SAOD value of 0.0001 because this is the value used during time periods without significant volcanic activity in that data set. We append the SAOD record of Sato et al. (1993) using the GloSSAC v2.2 data set. Below, we use these two appended VAI and SAOD records in alternate MLR and AF trend analysis cases.

2.1.4. El Niño Southern Oscillation

Variations in climate associated with the El Niño Southern Oscillation (ENSO) can have numerous effects on the global carbon cycle. ENSO indices used in our analysis appear in Figures 1e–1g, with El Niño and La Niña events appearing in red and blue, respectively, and neutral conditions shown in gray for the N1+2 (Eastern Pacific, 0–10° S, 90°W–80°W), N4 (Central Pacific, 5°N–5°S, 160°E−150°W), and N3.4 (Equatorial Pacific, 5°N–5°S, 170° W−120°W) indices. All ENSO indices are provided by NOAA's Climate Prediction Center (CPC) and are calculated from the Extended Reconstructed SST v5 data set (Huang et al., 2017). All ENSO indices have been linearly de-trended over the study period for use in our analysis.

During ENSO events, the growth rate of atmospheric CO_2 can be altered through shifts in weather patterns driven by variations in the Walker-Circulation. This perturbation leads to changes in surface temperature (Bradley et al., 1987), vapor pressure deficit (Brum et al., 2018), and precipitation patterns (Sasaki et al., 2015) that can affect plant growth (Keeling et al., 1996; Zhang et al., 2019). It is well established that global mean surface temperature rises during major El Niño events (Lean & Rind, 2008; McBride et al., 2021), which can increase plant respiration (Cavaleri et al., 2017), thus leading to an increase in the growth rate of atmospheric CO_2. Furthermore, significant El Niño events have been linked to an increase in wildfires in peat-rich regions such as Indonesia (Fuller & Murphy, 2006), resulting in a further increase in atmospheric CO_2 (van der Werf et al., 2008). Conversely, La Niña tends to produce cooler and wetter conditions in the tropics, which have suppressed the CO_2 growth rate in some years (Sellers et al., 2018). Finally, changes in sea surface temperature in the Equatorial Pacific can alter ocean outgassing of CO_2 (Chatterjee et al., 2017).

Several recent studies have examined the sensitivity of the carbon cycle to the type of ENSO, quantifying and comparing the effects of a Central Pacific (CP) and an Eastern Pacific (EP) ENSO index (Chylek et al., 2018; Teckentrup et al., 2021; Wang et al., 2018). In our MLR modeling analysis, we consider the use of both a CP and an EP ENSO index, N4 and N1+2, respectively, and a single ENSO index, Niño 3.4, as predictors for $dCO_2^{GLB-RAW}/dt$. The three ENSO indices examined in our analysis are all obtained from the Climate Prediction Center of the U.S. National Oceanic and Atmospheric Administration at https://www.cpc.ncep.noaa.gov/data/ indices/ersst5.nino.mth.91-20.ascii. Figure S3 in Supporting Information S1 shows scatter diagrams for each combination of the three indices. The CP and EP ENSO indices are weakly correlated ($R^2 = 0.21$), as they occupy different regions of the Equatorial Pacific, suggesting that both indices can be used as predictors in a single MLR model. We use the N3.4 index in alternate cases that rely on a single index to represent ENSO conditions.

We categorize the state of each ENSO index as El Niño, neutral, or La Niña in a manner similar to the classification used by NOAA's CPC, as explained below. To be considered an El Niño or La Niña event, the sea surface temperature anomaly of the index must remain above +0.5°C or below −0.5°C for five consecutive months. We use the monthly values for each ENSO index rather than the 3-month running mean of the Niño 3.4 index, which is used to classify ENSO conditions by NOAA's CPC. Separating ENSO into three phases is motivated by Sellers

et al. ([2018](#)), who document an asymmetric response of the growth rate of atmospheric CO_2 and AF to the El Niño, neutral, and La Niña conditions of ENSO. They showed that mean AF was highest during strong El Niño years, lowest during strong La Niña years, and that AF during neutral conditions tended to fall between values that occurred during strong El Niño and La Niña years. This behavior is explicitly represented in our model, described below, by computing regression coefficients for each of these three phases.

2.2. Multiple Linear Regression Analysis

In this analysis, we use a MLR model to quantify the contribution of natural variability attributed to ENSO conditions and major volcanic eruptions to the atmospheric CO_2 growth rate. For the baseline MLR case, the global modeled atmospheric CO_2 growth rate ($dCO_2^{GLB-MDL}/dt$), at each month i, is described by:

$$
\begin{aligned}
dCO_2^{GLB\text{-}MDL}/dt\,(i) = {} & C_0 + C_E * E_{TOT(i)} + C_V * SAOD_{(i)} + C_{CP\text{-}NINO} * N4_{NINO(i-9)} + C_{CP\text{-}NEU} * N4_{NEU(i-9)} \\
& + C_{CP\text{-}NINA} * N4_{NINA(i-9)} + C_{EP\text{-}NINO} * N12_{NINO(i-10)} + C_{EP\text{-}NEU} * N12_{NEU(i-10)} \\
& + C_{EP\text{-}NINA} * N12_{NINA(i-10)}
\end{aligned}
\tag{4}
$$

where E_{TOT} is the total sum of anthropogenic annual CO_2 emissions ($E_{FOS} + E_{LUC}$), including the cement carbonation sink, linearly interpolated to a monthly time grid, SAOD is the global mean stratospheric aerosol optical depth over land, N4 and N12 are the monthly CP and EP ENSO indices separated into three phases: El Niño (denoted NINO), and neutral (denoted NEU), and La Niña (denoted NINA), and i is the index of the time series in months. The regression coefficients are C_0, C_E, C_V, and $C_{CP\text{-}NINO}$, $C_{CP\text{-}NEU}$, $C_{CP\text{-}NINA}$, $C_{EP\text{-}NINO}$, $C_{EP\text{-}NEU}$, $C_{EP\text{-}NINA}$, corresponding to the regression constant and coefficients for total anthropogenic CO_2 emissions, volcanic influence, as well as the CP and EP ENSO separated into three phases, respectively. We use ENSO indices for the Central Pacific (CP) and Eastern Pacific (EP) in the baseline model; as noted in Section [2.1.4](#), these indices have only a small correlation which justifies the use of both indices. The numbers subtracted from the variable i in Equation [4](#) represent 9-month and 10-month lags for the CP and EP ENSO indices, respectively. The ENSO lags are discussed further below.

Figure [2](#) shows the output of the MLR analysis for our baseline simulation (Equation [4](#)). The top panel shows observed $dCO_2^{GLB-RAW}/dt$ in blue and the modeled global annual atmospheric CO_2 growth rate ($dCO_2^{GLB-MDL}/dt$) in green. Monthly values of $dCO_2^{GLB-RAW}/dt$ versus $dCO_2^{GLB-MDL}/dt$ exhibit a value of $R^2 = 0.77$, indicating this simple model approach captures more than three-quarters of the variability of monthly values of the atmospheric CO_2 growth rate. Contributions to variations in $dCO_2^{GLB-RAW}/dt$ from E_{TOT}, SAOD over land, the CP ENSO index (separated into El Niño, neutral, and La Niña phases), and the EP ENSO index (again separated into three phases) are shown in Figures [2b–2e](#). The gray shaded regions show the $\pm 1\sigma$ and $\pm 2\sigma$ standard deviations for each component of the regression computed using a conditional regression analysis (Denters & Van Pruijenbroek, [1989](#)).

As noted above, a 9-month and 10-month lag is used for the CP and EP ENSO indices in Equation [4](#). Following prior studies (Chylek et al., [2018](#); Gurney et al., [2012](#); Knorr, [2009](#); Raupach et al., [2008](#)), we have determined the lag for the ENSO indices based on maximizing the square of the correlation coefficient (R^2) between the observed detrended CO_2 growth rate and the ENSO indices. We detrend the observed CO_2 growth rate by regressing only the E_{TOT} variable against $dCO_2^{GLB-RAW}/dt$ and then subtracting the product of the resulting regression coefficient with the E_{TOT} variable from $dCO_2^{GLB-RAW}/dt$. Results from the ENSO lag analysis are shown in Figure S4 in Supporting Information [S1](#). The lags used in Equation [4](#) result in the largest value of R^2 for $dCO_2^{GLB-RAW}/dt$ versus $dCO_2^{GLB-MDL}/dt$. Similar analyses by Raupach et al. ([2008](#)), Knorr ([2009](#)), and van Marle et al. ([2022](#)), using a single ENSO index, found lags of 3 ± 1, 4, and 4 months respectively. Our lags differ by approximately 6 months from these previously published values because we define the time associated with CO_2 growth rate at the endpoint of the observations used in the calculation, as opposed to the midpoint (see Equation [3](#)). We do not use a time lag for E_{TOT} or SAOD in Equation [4](#) because the factors represented by these terms have a near instantaneous effect on the CO_2 growth rate.

A key aspect of our study is the use of the regression coefficients computed in the MLR model to account for natural variability arising from major volcanic eruptions and ENSO on the growth rate of atmospheric CO_2. We subtract the contributions of SAOD and ENSO to the CO_2 growth rate (lines in Figures [2c–2e](#)) from
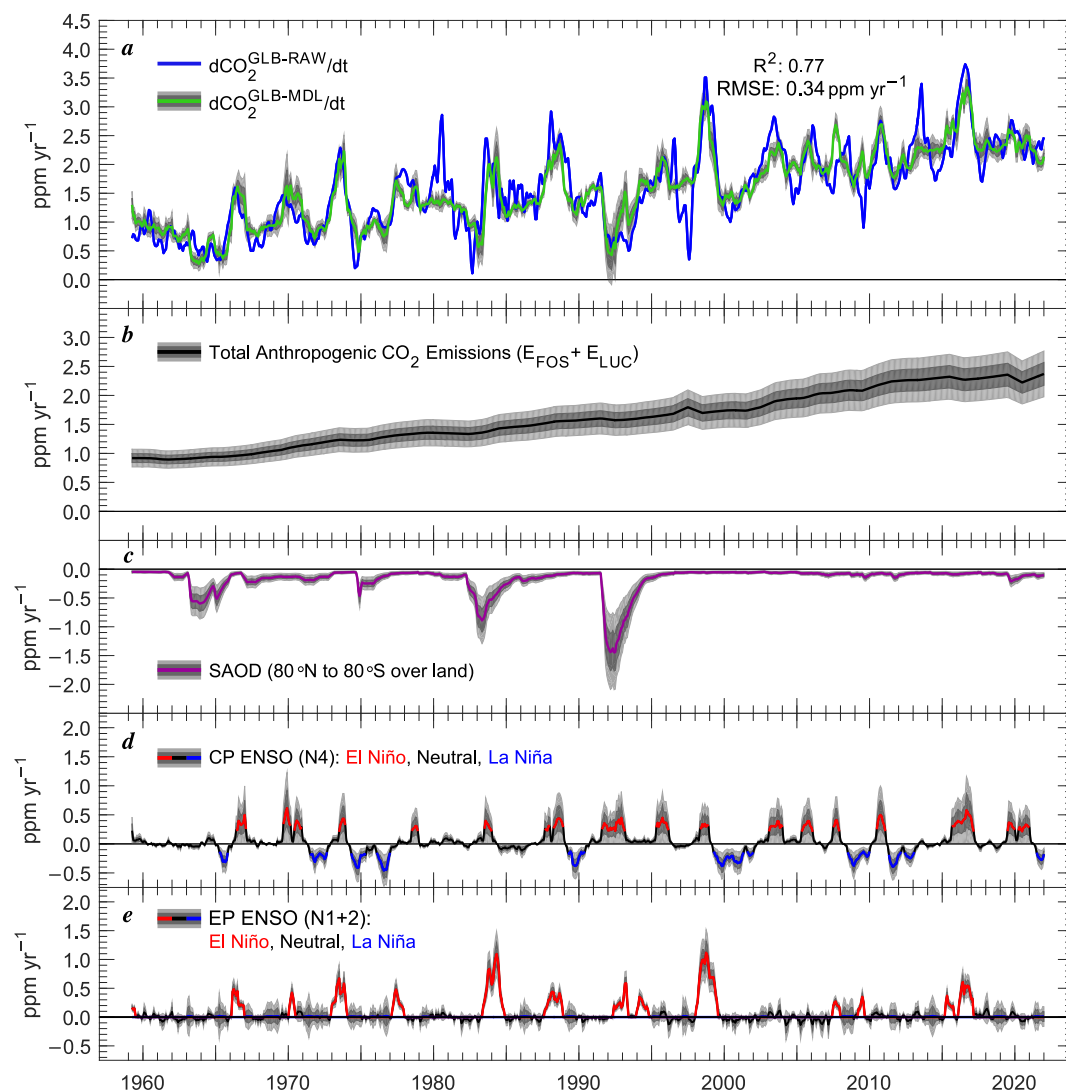
Figure 2. Measured and modeled atmospheric CO_2 growth rate. (a) Globally observed annual atmospheric CO_2 growth rate ($dCO_2^{GLB-RAW}/dt$) at a monthly time step (blue). Modeled annual atmospheric CO_2 growth rate ($dCO_2^{GLB-MDL}/dt$) at a monthly time step (green) attained from the MLR analysis on the basis of E_{TOT}, SAOD over land, and two ENSO indices; one for a CP ENSO (N4) and one for an EP ENSO (N1+2). (b) Contribution from total anthropogenic CO_2 emissions ($E_{FOS} + E_{LUC}$) to $dCO_2^{GLB-MDL}/dt$. (c) Contribution from SAOD over land to $dCO_2^{GLB-MDL}/dt$. (d) Contribution from CP ENSO (N4) to $dCO_2^{GLB-MDL}/dt$. (e) Contribution from EP ENSO (N1+2) to $dCO_2^{GLB-MDL}/dt$. Gray shaded regions are the $\pm 1\sigma$ and $\pm 2\sigma$ uncertainties for each regression variable found by conducting a conditional regression analysis.

$dCO_2^{GLB-RAW}/dt$ (blue line in Figure 2b) to attain a time series termed $dCO_2^{GLB-ADJ}/dt$, which is the global atmospheric CO_2 growth rate "adjusted" for natural variability, used in the AF trend analysis. The contributions of SAOD and ENSO to the CO_2 growth rate are found by multiplying the volcanic and ENSO regression coefficients with the underlying predictor time series for SAOD and ENSO (Figures 1d–1f). All AF trend analyses are conducted on an annual time grid. To place monthly $dCO_2^{GLB-ADJ}/dt$ on an annual time grid, we extract the data points corresponding to the end of the year, again to be consistent with formalism adopted by NOAA ESRL for their computation of the annual growth rate of CO_2. The resulting time series of $dCO_2^{GLB-ADJ}/dt$, shown by the thick blue line in Figure 3c, is used prominently in the following trend analysis.

Table 1 describes the 11 MLR modeling cases used in our AF trend analysis. Alternate cases are examined to quantify the sensitivity of various MLR modeling approaches on the AF trend analysis. In these alternate cases, we vary the model time grid (monthly or annual), the data sources of the SAOD time series, and the ENSO indices when modeling the CO_2 growth rate observed either globally or at MLO. The first case is described
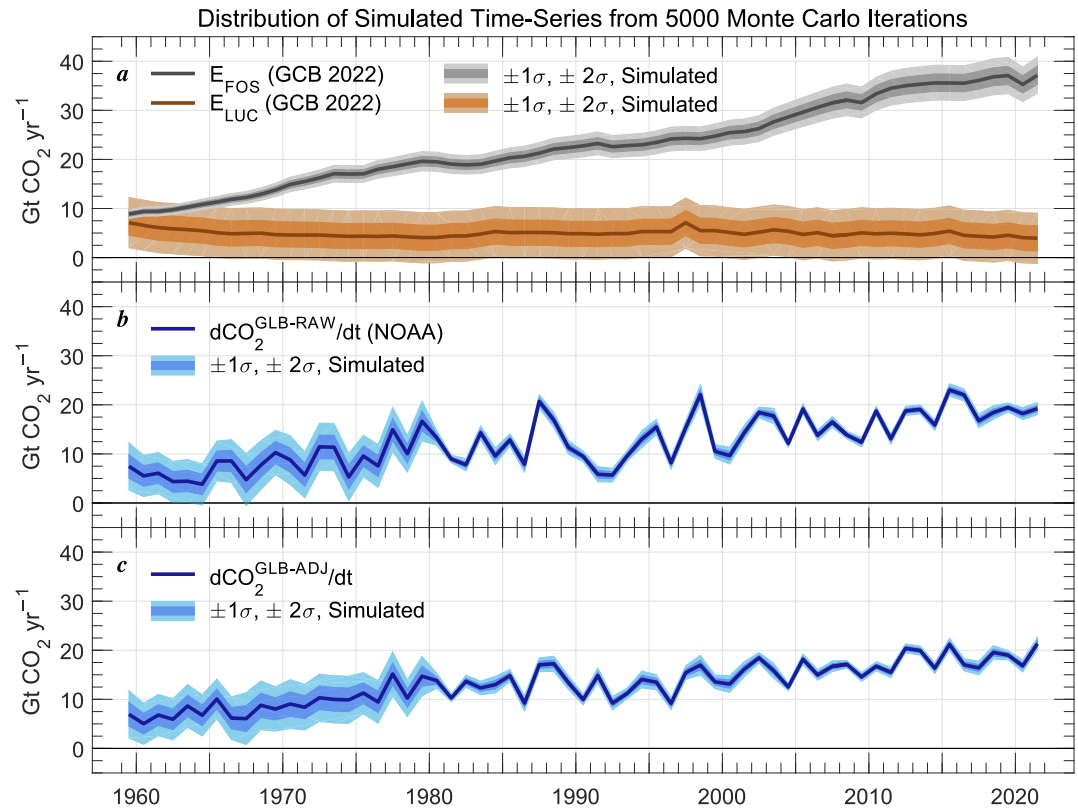
Figure 3. Distribution of synthetic time series from Monte Carlo (MC) simulations. (a) E_{FOS}, including the cement carbonation sink, (black line) and E_{LUC} (brown line) reported by the GCB 2022. The shaded regions show the distribution of the $\pm1\sigma$ and $\pm2\sigma$ standard deviations of the 5000 synthetic time series from the MC analysis that incorporates a first-order AR model for E_{FOS} and E_{LUC}. (b) Global $dCO_2^{GLB-RAW}/dt$ (blue line) from NOAA ESRL. The shaded regions show the $\pm1\sigma$ and $\pm2\sigma$ standard deviations of the 5000 synthetic time series from the MC analysis for $dCO_2^{GLB-RAW}/dt$. (c) Same as (b), except for $dCO_2^{GLB-ADJ}/dt$.

Table 1
MLR Modeling Cases Used in Our Study

	dCO_2/dt	Time grid	SAOD	ENSO
Case 1	GLB	Monthly	CMIP6-GloSSAC	CP & EP
Case 2	GLB	Monthly	CMIP6-GloSSAC	N3.4
Case 3	GLB	Annual	CMIP6-GloSSAC	CP & EP
Case 4	GLB	Annual	CMIP6-GloSSAC	N3.4
Case 5	MLO	Monthly	CMIP6-GloSSAC	CP & EP
Case 6	MLO	Monthly	CMIP6-GloSSAC	N3.4
Case 7	MLO	Annual	CMIP6-GloSSAC	CP & EP
Case 8	MLO	Annual	CMIP6-GloSSAC	N3.4
Case 9	GLB	Monthly	CMIP6-GloSSAC (no land fraction weighting)	CP & EP
Case 10	GLB	Monthly	VAI, Ammann et al. (2003a, 2003b)	CP & EP
Case 11	GLB	Monthly	Sato et al. (1993)	CP & EP

Note. Case 1 is the baseline case shown by Equation 4 and results in Figure 2. The various MLR cases predict either the global CO_2 growth rate or the CO_2 growth rate observed at MLO, on either a monthly or annual time grid, with the CMIP6-GloSSAC record, with and without land fraction weighting, the VAI of Ammann et al. (2003a, 2003b) or SAOD from Sato et al. (1993), and the use of both a Central Pacific (CP) and Eastern Pacific (EP) ENSO index or only the N3.4 ENSO index.

mathematically by Equation 4. Case 2 differs from case 1 by using only a single ENSO index (N3.4) to represent conditions in the Equatorial Tropical Pacific. Cases 3 and 4 are similar to cases 1 and 2, except the MLR is conducted on an annual rather than monthly time grid. When modeling the CO_2 growth rate on a monthly time grid, each ENSO index is separated into the three phases (NINO, NEU, and NINA) described above. When modeling the CO_2 growth rate on an annual time grid, we use annual averages for global SAOD over land and lagged annual averages for ENSO. Subsequently, in the annual MLR cases, ENSO is not separated into phases. Cases 5 through 8 are analogous to cases 1 through 4, respectively, except we model the CO_2 growth rate at MLO as opposed to the global CO_2 growth rate. Cases 9 through 11 are identical to our baseline case (case 1), except the influence of volcanoes is determined by alternate time series of SAOD. In case 9 the CMIP6-GloSSAC record is used without latitudinal land fraction weighting. In cases 10 and 11 the VAI of Ammann et al. (2003a, 2003b) and SAOD of Sato et al. (1993) are used, respectively. The governing equations and figures depicting model output for additional cases appear in Supporting Information S1. Finally, we repeat the baseline analysis with the 20 additional E_{LUC} estimates (the three bookkeeping models, the 16 DGVMs, and the mean of the 16 DGVMs) and one case without an estimate for E_{LUC} to calculate trends in AF determined only from E_{FOS}.

2.3. Monte Carlo Simulations

We examine the full range of uncertainties for each component of the CO_2 AF to accurately assess the statistical significance of the resulting trends. To account for the uncertainties, we use a Monte Carlo (MC) analysis coupled with a first-order autoregressive (AR) model to generate synthetic time series of E_{FOS}, E_{LUC}, $dCO_2^{GLB-RAW}/dt$, and $dCO_2^{GLB-ADJ}/dt$, similar to the approach of Ballantyne et al. (2015). The black and brown lines in Figure 3a show E_{FOS} and E_{LUC} from GCB 2022 (Friedlingstein, et al., 2022). The shaded regions in Figure 3a show the distribution of the $\pm 1\sigma$ and $\pm 2\sigma$ standard deviations of the computed time series from 5000 MC iterations found using our AR model, as described below. The blue lines in Figures 3b and 3c show $dCO_2^{GLB-RAW}/dt$ as provided by NOAA (Section 2.1.2) and $dCO_2^{GLB-ADJ}/dt$ we find using our MLR model (Section 2.2). Similarly, the shaded regions in Figures 3b and 3c show the $\pm 1\sigma$ and $\pm 2\sigma$ standard deviations of the 5000 time series for $dCO_2^{GLB-RAW}/dt$ and $dCO_2^{GLB-ADJ}/dt$ computed by our MC analysis.

Here we provide further details of our MC analysis that we use to quantify the uncertainty in trends of AF. We conduct MC simulations to generate 5000 synthetic time series, where the annual standard deviation of the probability distribution at each time step of the 5000 generated time series matches the published uncertainty of the respective component of AF. This method enables the full range of uncertainties to be considered when analyzing the trends in AF. Autoregressive models are commonly used in MC simulations for time series analysis because their inclusion allows for error retention in previous time steps to be propagated forward. We examine the autocorrelation functions (ACF) and partial autocorrelation functions (PACF) to determine whether an AR model should be included in the MC analysis, and to specify the order of the AR model if used. The ACF and PACF of the linearly detrended time series of E_{FOS}, E_{LUC}, $dCO_2^{GLB-RAW}/dt$, and $dCO_2^{GLB-ADJ}/dt$ as well as the uncertainty time series for dCO_2^{GLB}/dt are shown in Figure S15 in Supporting Information S1. A first-order AR model is included in the MC simulations to generate synthetic time series of E_{FOS}, E_{LUC}, $dCO_2^{GLB-RAW}/dt$, and $dCO_2^{GLB-ADJ}/dt$. Figure S15 in Supporting Information S1 displays the autocorrelated behavior of E_{FOS}, E_{LUC}, and the uncertainty time series associated with dCO_2^{GLB}/dt. We use the 95% confidence bounds (i.e., twice the standard error) of the PACFs to determine the order of the AR model. A first-order AR model is chosen for E_{FOS} and E_{LUC} in the MC simulations because the partial autocorrelation values fall substantially outside the confidence bounds at a lag of 1 year (Figures S15f and S15g in Supporting Information S1).

Equations 5 and 6 describe the AR models used to generate time series of E_{FOS} and E_{LUC},

$$X_{FOS_{(t)}} = (E_{FOS_{(t)}} + \phi * (X_{FOS_{(t-1)}} - E_{FOS_{(t-1)}}) + \varepsilon_{FOS_{(t)}}) * \frac{\sigma_{EFOS(t)}}{\sigma_{XFOS(t)}} \tag{5}$$

$$X_{LUC(t)} = (E_{LUC_{(t)}} + \phi * (X_{LUC_{(t-1)}} - E_{LUC_{(t-1)}}) + \varepsilon_{LUC_{(t)}}) * \frac{\sigma_{ELUC(t)}}{\sigma_{XLUC(t)}} \tag{6}$$

where $X_{FOS}(t)$ and $X_{LUC}(t)$ are the modeled synthetic time series of E_{FOS} and E_{LUC}, $E_{FOS}(t)$ and $E_{LUC}(t)$ are the anthropogenic CO_2 emissions at time t in years, ϕ is the AR coefficient. The AR coefficient enables the synthetic time series to retain a portion of the error from previous years. In a first-order AR process, ϕ is simply the autocorrelation (R) at a lag of 1 year. Here, the AR coefficients are 0.90 for E_{FOS} and 0.68 for E_{LUC} (Figure S15 in Supporting Information S1). The terms $\varepsilon_{FOS}(t)$ and $\varepsilon_{LUC}(t)$ represent the randomly generated newly introduced error, at time t, following a normal distribution. The $\varepsilon_{FOS}(t)$ term uses the total uncertainty of $\pm5\%$ of $E_{FOS}(t)$ to generate the normally distributed error. The $\varepsilon_{LUC}(t)$ term, for the three E_{LUC} bookkeeping models and their average, uses the semi-quantitative uncertainty of ±2.57 GtCO$_2$ yr^{-1} to generate the normally distributed error for each year. The $\varepsilon_{LUC}(t)$ term, for the 16 DGVM E_{LUC} and their multi-model mean, uses a quantitative uncertainty of 2.05 GtCO$_2$ yr^{-1} to generate the normally distributed error for each year. The values used to generate the normally distributed error for E_{FOS} and the bookkeeping E_{LUC} time series are given by GCB 2022. The value used to generate the normally distributed error for the 16 DGVM E_{LUC} and their multi-model mean is the mean of the annual standard deviation of the 16 DGVMs. The final terms in Equations 5 and 6, $\sigma_{EFOS(t)}$ and $\sigma_{ELUC(t)}$ divided by $\sigma_{XFOS(t)}$ and $\sigma_{XLUC(t)}$, are the uncertainties for E_{FOS} and E_{LUC}, noted just above, divided by the standard deviation of the 5000 simulations of X_{FOS} and X_{FOS}, at time t. Using this final weighting term ensures that the statistical distribution of the standard deviation of the simulated time series of $X_{FOS}(t)$ and $X_{LUC}(t)$ matches the uncertainties given by GCB 2022 for E_{FOS} and for the bookkeeping E_{LUC}, as well as the uncertainty we calculate for the DGVM E_{LUC}. We do not account for any uncertainty in the cement carbonation sink within the MC analysis, because the magnitude of this sink is less than half of the 1σ uncertainty attributed to E_{FOS}. Instead, we simply subtract the cement carbonation sink time series from the 5000 synthetic E_{FOS} time series generated in the MC analysis.

We use a MC analysis with a first-order AR model to generate 5000 synthetic time series of $dCO_2^{GLB-RAW}/dt$, $dCO_2^{GLB-ADJ}/dt$, $dCO_2^{MLO-RAW}/dt$, and $dCO_2^{MLO-ADJ}/dt$. The blue lines in Figures 3b and 3c show $dCO_2^{GLB-RAW}/dt$ and $dCO_2^{GLB-ADJ}/dt$, where the blue shading represents the $\pm1\sigma$ and $\pm2\sigma$ standard deviations of the synthetic time series. Here, a first-order AR model is used to generate the synthetic time series, because the ACF and PACF of the uncertainty time series associated with dCO_2/dt exhibit values that fall outside the 95% confidence bounds (Figure S15 in Supporting Information S1). Each synthetic time series for the raw and adjusted CO_2 growth rate for the globe and at MLO is generated by the equation:

$$X_{\frac{dCO_2}{dt}(t)} = \left(\frac{dCO_2}{dt}_{(t)} - \phi * \left(X_{\frac{dCO_2}{dt}(t-1)} - \frac{dCO_2}{dt}_{(t-1)}\right) + \varepsilon_{\frac{dCO_2}{dt}(t)}\right) * \frac{\sigma_{\frac{dCO_2}{dt}(t)}}{\sigma_{X\frac{dCO_2}{dt}(t)}} \qquad (7)$$

where $XdCO_2/dt(t)$ is the MC model simulated synthetic time series for either $dCO_2^{GLB-RAW}/dt$, $dCO_2^{GLB-ADJ}/dt$, $dCO_2^{MLO-RAW}/dt$, or $dCO_2^{MLO-ADJ}/dt$, at time t, where the first term on the right hand side is either the time series of $dCO_2^{GLB-RAW}/dt$, $dCO_2^{GLB-ADJ}/dt$, $dCO_2^{MLO-RAW}/dt$, or $dCO_2^{MLO-ADJ}/dt$, at time t, and ϕ is the AR coefficient. Here, the difference between the synthetic time series and the observed CO_2 growth rate at the previous time step is multiplied by ϕ and subtracted from dCO_2/dt, using a value for the AR coefficient ϕ of 0.98 (Figure S15j in Supporting Information S1). Errors that are biased high (or low) in the prior year result in estimates of dCO_2/dt that are biased low (or high) in subsequent years, resulting in synthetic time series for dCO_2/dt that are reflective of actual atmospheric observations. The $\varepsilon_{dCO2/dt}(t)$ term represents the newly introduced randomly generated error following a normal distribution at time t, where t is in years, that is then added to generate the synthetic time series. The final terms in Equation 7, $\sigma_{dCO2/dt}(t)$ divided by $\sigma_{XdCO2/dt}(t)$ is the uncertainty for $dCO_2/dt(t)$ divided by the standard deviation of the 5000 simulated time series for $X_{dCO2/dt}(t)$. The final weighting term ensures that the statistical distribution of the standard deviation of the simulated time series for $X_{dCO2/dt}(t)$ match the uncertainties given by NOAA. To generate the normally distributed random error for the raw and adjusted global CO_2 growth rate for every year, we use a time series of the estimated uncertainty for $dCO_2^{GLB-RAW}/dt$ provided by NOAA (Ballantyne et al., 2012; Conway et al., 1994), shown as the gray shading in Figure 1b. To generate the normally distributed random error for the raw and adjusted CO_2 growth rate at MLO for every year, we use an estimated uncertainty for $dCO_2^{MLO-RAW}/dt$ of ±0.11 ppm yr^{-1} provided by NOAA (Keeling et al., 1976), https://gml.noaa.gov/ccgg/trends/gr.html. The estimated uncertainty for the CO_2 growth rate observed at MLO is constant from year to year. In contrast, the estimated uncertainty for the global CO_2 growth rate is relatively high before 1980 and decreases toward the present, as discussed in Section 2.1.1.

3. Results and Discussion

3.1. Multiple Linear Regression

We use a MLR to model the atmospheric CO_2 growth rate ($dCO_2^{GLB-RAW}/dt$). Figure 2 shows the output for our baseline scenario (case 1), as described by Equation 4 in Section 2.2. This simulation results in a value of 0.77 for the correlation coefficient (R^2) and 0.34 ppm yr^{-1} for the root mean squared error (RMSE) of modeled versus observed atmospheric CO_2 growth rate from 1959 to 2021. The inclusion of proxies for the effect of ENSO and major volcanic eruptions on $dCO_2^{GLB-RAW}/dt$ is a significant factor leading to such a strong correlation between the modeled and measured growth rate. When terms for ENSO and volcanic eruptions are removed from the regression, R^2 falls to 0.53 and RMSE rises to 0.49 ppm yr^{-1} (this simulation is not shown).

The global carbon cycle is strongly affected by conditions in the Tropical Pacific Ocean during El Niño events, leading to an increase in the global atmospheric CO_2 growth rate. Table S1 in Supporting Information S1 shows the regression coefficients for the baseline MLR simulation, which includes indices for both the Central Pacific (CP ENSO, the N4 index) and the Eastern Pacific (EP ENSO, the N1+2 index). The effect of Tropical Pacific conditions on $dCO_2^{GLB-RAW}/dt$ is evident from the sharp upward deviations in the CO_2 growth rate during major El Niño events (Figures 2d and 2e). The more rapid growth in atmospheric CO_2 is caused by precipitation and temperature anomalies that suppress plant growth in the tropics (Betts et al., 2016; Jones & Cox, 2005; Keeling et al., 1995), changes in plant respiration in the tropics associated with nighttime warming (Anderegg et al., 2015), as well as the particularly intense peatland fires in Southeast Asia during the 1998 El Niño event (Fuller & Murphy, 2006). Tropical peatland fires during other El Niño events have had a smaller but noticeable effect on the CO_2 growth rates (Pan et al., 2018; van der Werf et al., 2008). When the Central Tropical Pacific is in a La Niña phase, the CO_2 growth rate is slightly suppressed relative to neutral conditions (Figure 2d). If we replace the N4 (CP ENSO) and N1+2 (EP ENSO) with the N3.4 index, R^2 falls slightly from 0.77 to 0.76 and RMSE rises slightly from 0.34 to 0.35 ppm yr^{-1}, as shown on Figure 2 and Figure S5 in Supporting Information S1. Our scientific findings regarding the trends in the airborne fraction of CO_2 (AF) are unaffected if we use the N3.4 index rather than the N4 and N1+2 indices. The inclusion of two indices representing the cumulative effect of ENSO on the CO_2 growth rate in our baseline MLR simulation is motivated by recent studies that report differing responses in various components of the carbon cycle to El Niño events originating in the Central or Eastern Pacific (Chylek et al., 2018; Pan et al., 2018; Teckentrup et al., 2021; Wang et al., 2018).

For our baseline simulation, the time series for $dCO_2^{GLB-RAW}/dt$ is adjusted for the impact of conditions in the Tropical Pacific using the modeled influences shown in Figures 2d and 2e. The CP and EP ENSO indices differ considerably (Figures 1e and 1f). The expression of variations in $dCO_2^{GLB-RAW}/dt$ to these indices is strongest when the Eastern Pacific is in an El Niño condition (Figure 2e). Variations in $dCO_2^{GLB-RAW}/dt$ respond to La Niña conditions more strongly with respect to the CP index than the EP index. When terms for ENSO are removed from the regression, R^2 falls from 0.77 to 0.58 and RMSE rises from 0.34 to 0.47 ppm yr^{-1}.

An analysis of observed carbon cycle-climate feedbacks by Sellers et al. (2018) reported an asymmetric response in the magnitude of AF to El Niño, neutral, and La Niña conditions. Regression coefficients calculated in our MLR analysis for all monthly cases (shown in Table S1 in Supporting Information S1 for our baseline case and alternate monthly cases 2, 5, 6, 9, 10, and 11 on Figures S5, S8, S9, S12–S14 shown in Supporting Information S1) also exhibit an asymmetry in their magnitude. In each monthly case, regression coefficients for El Niño phases of the CP ENSO (N4) and N3.4 indices are roughly 1.5 to 3 times greater than the corresponding regression coefficients for neutral and La Niña conditions. For the EP ENSO (N1+2 index), regression coefficients for La Niña conditions are approximately 10 times smaller than the El Niño regression coefficient. On a global scale, the terrestrial biosphere assimilates atmospheric CO_2 at a steadier rate during La Niña and neutral years compared to El Niño conditions.

The growth rate of atmospheric CO_2 is reduced following major volcanic eruptions. Several eruptions strong enough to reach the stratosphere over the study period, such as El Chichón in 1982 and Mount Pinatubo in 1991, led to sharp enhancements in stratospheric aerosol optical depth (SAOD) that persisted for several years (Figure 1d). During periods of elevated SAOD, photosynthesis increases (Gu et al., 2003; Raupach et al., 2014; van Marle et al., 2022) due to a dramatic increase in the ratio of diffuse to direct solar irradiance reaching the surface (Dutton & Bodhaine, 2001; Dutton & Christy, 1992). The influence of SAOD on $dCO_2^{GLB-RAW}/dt$ computed using our MLR model is shown in Figure 2c. Following the eruption of Mount Pinatubo, we estimate

that the CO_2 growth rate in 1991 was suppressed by about 1.3 ± 0.3 ppm yr^{-1}. The eruptions of Mount Agung, Fuego, and El Chichón in 1963, 1974, and 1982, respectively, led to similar reductions in the CO_2 growth rate due to photosynthetic enhancement caused by stratospheric aerosols (Figures 1d and 2c). The magnitude of the suppression of $dCO_2^{GLB-RAW}/dt$ following these eruptions is comparable to the annual atmospheric CO_2 growth rate. Consequently, in the analysis described in Section 3.2, the time series for $dCO_2^{GLB-RAW}/dt$ is adjusted for the impact of major volcanic eruptions using the modeled influence shown in Figure 2c. The volcanic adjustment is critical to the proper determination of the trends in AF because each of the major eruptions that substantially enhanced SAOD occurred during the first 32 years of the 62-year data record. When the SAOD term is removed from the regression, R^2 falls from 0.77 to 0.68 and RMSE rises from 0.34 to 0.40 ppm yr^{-1}.

When an alternate time series for SAOD based upon the CMIP6-GloSSAC record without latitudinal weighting by global land fraction, the VAI record of Ammann et al. (2003a, 2003b), or the SAOD data set of Sato et al. (1993) (Section 2.1.3) are used in an MLR to model the atmospheric CO_2 growth rate, the model performance results in R^2 values of 0.77, 0.76, and 0.76, respectively (cases 9–11 shown in Figures S12–S14 in Supporting Information S1). These values of R^2 are the same or slightly lower than the value in the baseline simulation. Our scientific findings regarding the statistical significance of the trends in AF are unaffected by our choice of SAOD record. We use the CMIP6-GloSSAC record for SAOD to be consistent with many emergent studies (Malik et al., 2017; Sellar et al., 2020; Toohey et al., 2016) that are using the volcanic forcing data set of Arfeuille et al. (2014) and also because the Ammann et al. (2003a, 2003b) VAI record ends in 1999 and the Sato et al. (1993) SAOD record ends in 2012, and to our knowledge have not been updated.

3.2. Airborne Fraction Trend Analysis

3.2.1. Baseline Modeling Case

We analyze trends in the airborne fraction of atmospheric CO_2 (AF) to quantify possible changes in the combined magnitude of the global terrestrial and oceanic carbon sinks over the study period (1959–2021). Trends in AF are computed using two representations of the global atmospheric CO_2 growth rate: $dCO_2^{GLB-RAW}/dt$ (raw data shown in Figures 2a and 3b) and $dCO_2^{GLB-ADJ}/dt$ (data adjusted for the influences of conditions in the Tropical Pacific as well as major volcanic eruptions). The time series of $dCO_2^{GLB-ADJ}/dt$ central to the analysis that follows is shown by the dark blue line in Figure 3c. The adjusted time series displays a smoother rise in the atmospheric growth rate of CO_2 compared to the raw data. Adjustments to the CO_2 growth rate due to conditions in the Tropical Pacific and major volcanic eruptions are a common element of prior analyses that have quantified trends in AF (Canadell et al., 2007; Knorr, 2009; Le Quéré et al., 2009; Raupach et al., 2008, 2014; van Marle et al., 2022).

Figure 4 summarizes the results of our AF trend analysis for the baseline case. Figure 4a shows the time series of AF (Equation 2) based upon the CO_2 global growth rate (AF$^{GLB-RAW}$) unadjusted for ENSO and volcanoes, as well as a linear fit to this time series. Figure 4b shows AF for the CO_2 global growth rate time series adjusted for the influence of ENSO and volcanoes (AF$^{GLB-ADJ}$). Slopes for each AF time series shown in Figure 4 are found using a linear least square fit to the respective data; slopes are expressed in units of yr^{-1} since the AF time series is dimensionless. Figure S16 in Supporting Information S1 shows an analysis similar to that of Figure 4, for values of the Sen's slope (Sen, 1968), which is the median of all combinations of pairwise slopes between data points. The same scientific conclusion, described below, is drawn from either figure.

We initially focus on the time period 1959 to 2021, for which the slopes of AF$^{GLB-RAW}$ and AF$^{GLB-ADJ}$ have values of 0.0009 yr^{-1} and -0.0001 yr^{-1}, respectively. Similar values of 0.0011 yr^{-1} and 0.0001 yr^{-1} are found for the associated Sen's slopes. The linear least square fit to the raw CO_2 data, resulting in a value of 0.0009 yr^{-1} for AF$^{GLB-RAW}$, implies a rise in the airborne fraction of CO_2 from 0.42 in 1959 to 0.48 in 2021. This rise, if true, would indicate a significant decline in the relative efficacy of the combined global terrestrial biosphere and oceanic carbon sinks for the sequestration of anthropogenic CO_2. A rise in AF using an analysis based only on raw data (i.e., not adjusted for the influence of ENSO and volcanoes) has been reported by Ballantyne et al. (2012, 2015) and Bennedsen et al. (2019). Based on the rise in AF, both studies noted a possible decline in the efficiency of carbon uptake by the combined global terrestrial and oceanic sinks. However, this decline was not statistically significant at the 95% confidence level in either study.
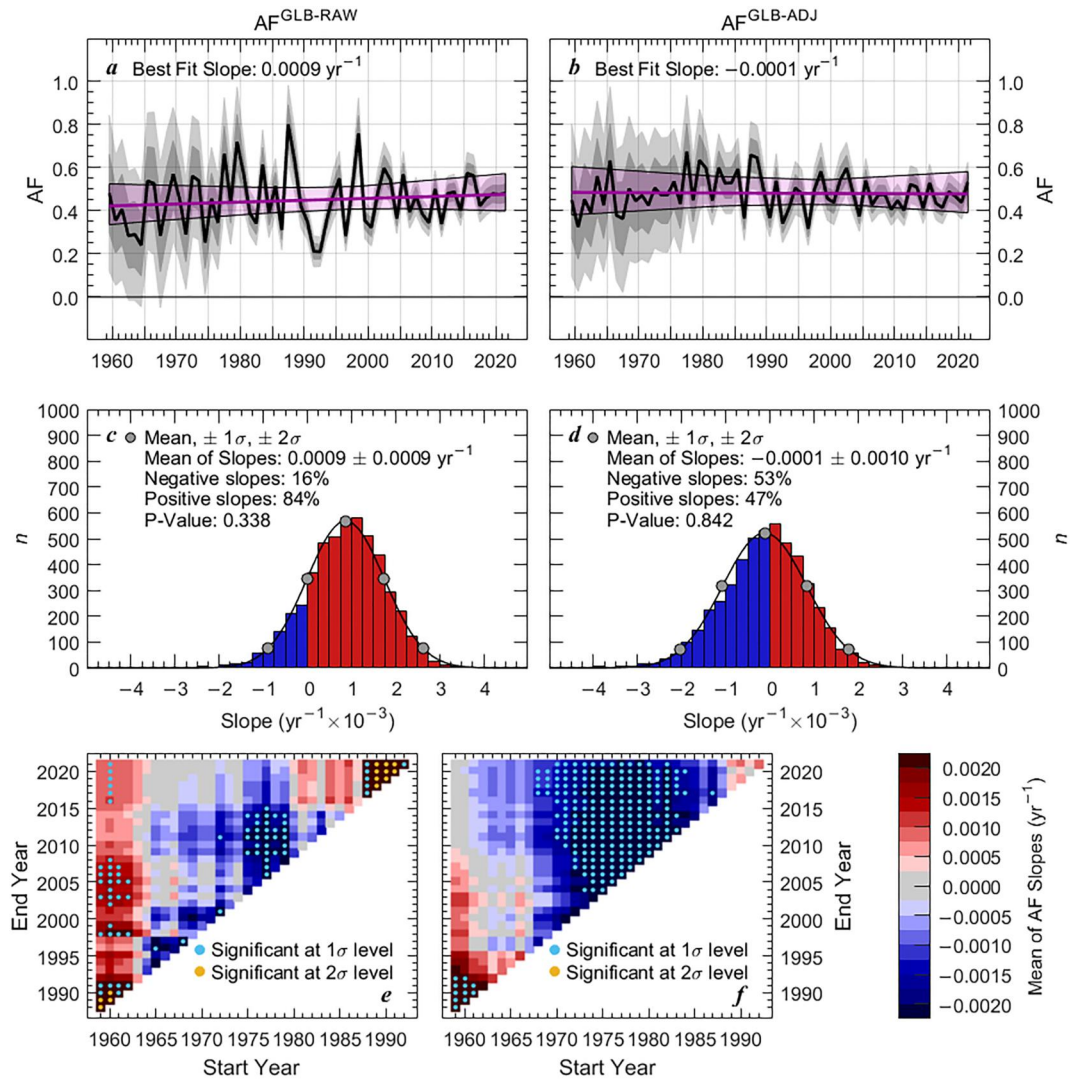
Figure 4. (a) Global CO_2 airborne fraction ($AF^{GLB-RAW}$) (black) and best fit trendline (purple). Gray shading shows the $\pm 1\sigma$ and $\pm 2\sigma$ standard deviations for the 5000 synthetic time series of $AF^{GLB-RAW}$ generated from the MC analysis of $dCO_2^{GLB-RAW}/dt$, E_{FOS}, and E_{LUC}. The light purple shading represents the $\pm 2\sigma$ slope uncertainty. (b) Same as (a), except for $AF^{GLB-ADJ}$ calculated using $dCO_2^{GLB-ADJ}/dt$. (c) The probability distribution function of the 5000 $AF^{GLB-RAW}$ slopes, binned as shown. Red bars show positive slopes, and blue bars show negative slopes. Gray circles denote the mean (center) and $\pm 1\sigma$ and $\pm 2\sigma$ standard deviations. (d) Same as (c), except for $AF^{GLB-ADJ}$. (e) Sensitivity of trend analysis to start and end years of the linear regression. The colored squares show the mean of the 5000 $AF^{GLB-RAW}$ slopes from the MC analysis, for the corresponding start and end years on the x and y-axes. (f) Same as (e) except for the analysis of $AF^{GLB-ADJ}$. The teal and gold dots on panels (e, f) denote the slopes that are statistically significant from 0 at the 1σ and 2σ level, respectively.

Figure 4b shows reduced interannual variability (IAV) for the AF time series adjusted for ENSO and volcanoes compared to the raw AF time series. The reduction in IAV is most apparent in 1991 and 1992 due to the upward revision of $AF^{GLB-ADJ}$ following the eruption of Mount Pinatubo, as well as in 1987 and 1998 due to the downward revision of $AF^{GLB-ADJ}$ following two major El Niño events. The El Niño event of 1982–1983 and the enhancement in SAOD during 1982 and 1983 due to the eruption of El Chichón had offsetting impacts on the CO_2 growth rate (Figures 1 and 2). Consequently, the time series for $AF^{GLB-ADJ}$ is similar to the time series of $AF^{GLB-RAW}$ in the early 1980s. As noted in the prior paragraph, the slope of $AF^{GLB-ADJ}$ is -0.0001 yr^{-1} for the 1959 to 2021 time period. The contrast between this slope and the rise in AF of 0.0009 yr^{-1} found for the raw data highlights the importance of accounting for the impact of natural variability on the CO_2 growth rate to determine whether the combined global terrestrial biosphere and oceanic sinks are changing. An AF slope of -0.0001 yr^{-1},

if true, would imply either little observable change or perhaps a slight enhancement in the efficacy of the combined carbon sinks for the sequestration of anthropogenic CO_2 over the study period.

We conduct a Monte Carlo (MC) analysis to assess the statistical significance of the trends in $AF^{GLB-RAW}$ and $AF^{GLB-ADJ}$. Details of the MC analysis, which consists of the generation of 5000 synthetic time series for the raw and adjusted CO_2 growth rate, E_{FOS}, and E_{LUC}, are given in Section 2.3. The light and dark gray shading in Figure 4a show the $\pm1\sigma$ and $\pm2\sigma$ standard deviation of the distribution of $AF^{GLB-RAW}$ from the MC analysis. The greater uncertainty in $AF^{GLB-RAW}$ early in the period of study (1959–1980) compared to the later part of the record (1990–2021) reflects the increased precision in quantifying the atmospheric CO_2 growth rate as the number and global distribution of monitoring stations has risen over the past six decades. Figure 4b shows results from the MC analysis for $AF^{GLB-ADJ}$ (i.e., the use of $dCO_2^{GLB-ADJ}/dt$ rather than $dCO_2^{GLB-RAW}/dt$). The purple shading shown in Figures 4a and 4b represents the distribution of trendlines of the synthetic AF time series with slopes that fall within $\pm2\sigma$ of the mean of the 5000 synthetic slopes.

Figures 4c and 4d show the probability distribution function (PDF) of the slopes for the 5000 synthetic time series of $AF^{GLB-RAW}$ and $AF^{GLB-ADJ}$, respectively. Positive slopes are shown in red and negative slopes in blue, with gray circles denoting the mean and the $\pm1\sigma$ and $\pm2\sigma$ standard deviations of the 5000 slopes. The analysis of $AF^{GLB-RAW}$ in Figure 4c shows that 84% of the simulations have positive slopes, whereas the analysis of $AF^{GLB-ADJ}$ in Figure 4d shows 47% of the simulated time series have positive slopes. The mean and $\pm1\sigma$ of the 5000 slopes are 0.0009 ± 0.0009 yr^{-1} for $AF^{GLB-RAW}$ and -0.0001 ± 0.0010 yr^{-1} for $AF^{GLB-ADJ}$. The trends in AF can also be expressed in units of % yr^{-1}, which we use for comparison with prior studies that report trends in this manner (Canadell et al., 2007; Frölicher et al., 2013; Le Quéré et al., 2009; Raupach et al., 2008, 2014). We use the same method as Frölicher et al. (2013) to calculate trends as a percentage. To determine the trend as a percentage, we multiply the slope calculated in the ordinary least squares linear regression by the length of the AF time series and divide by the mean of AF for the particular time series. When expressed as a % yr^{-1}, the mean and standard deviation of the slopes from the MC analysis are 0.12 ± 0.12% yr^{-1} for $AF^{GLB-RAW}$ and -0.01 ± 0.12% yr^{-1} for $AF^{GLB-ADJ}$.

The solid black line on Figures 4c and 4d show a Gaussian constrained to match the mean, $\pm1\sigma$, and $\pm2\sigma$ standard deviations of the 5000 slopes found in the MC analysis. Since the positive slopes on Figure 4c start near the -1σ region of the Gaussian, this simple analysis suggests that positive slopes for the unadjusted data may be statistically significant at the 1σ (68%) level. However, the positive slopes for the unadjusted data are not significant at the 2σ (95%) level. The MC analysis of the adjusted data shown in Figure 4d yields nearly an equal split between positive and negative slopes. Figures 4c and 4d also show the P-values calculated using the Mann-Kendall (MK) test (Kendall, 1948; Mann, 1945) for the $AF^{GLB-RAW}$ and $AF^{GLB-ADJ}$ time series shown in Figures 4a and 4b. The MK test is a commonly used test statistic in time series analysis to determine whether or not a monotonic positive or negative trend is present. The MK P-values shown on both panels are much greater than the commonly used 0.05 significance threshold. The PDFs and P-value analysis both imply that the trends in AF are not significant at the 2σ (95%) level for either the raw or adjusted data. The results from our trend analysis support the findings of Ballantyne et al. (2012, 2015) and Bennedsen et al. (2019) that the trend in $AF^{GLB-RAW}$ is positive, but not statistically different from 0 at the 2σ level. Furthermore, our results are also in agreement with studies by Knorr (2009) and Frölicher et al. (2013) that the trend in $AF^{GLB-ADJ}$ decreases when accounting for natural variability due to ENSO and volcanoes, but is also not statistically different from 0 at the 2σ level.

We next examine how the trend in AF varies as a function of the start and end year. This analysis is conducted to quantify the robustness of the slopes in AF, described above, to this most essential detail (Medhaug et al., 2017) and to facilitate the comparison of our findings to those in the literature, which examine data for a range of time periods. Figures 4e and 4f show the mean slopes of $AF^{GLB-RAW}$ and $AF^{GLB-ADJ}$ as a function of start (x-axis) and end year (y-axis). Only time frames that cover 30 or more years are considered. The mean slopes shown in Figures 4e and 4f are found using the same 5000 synthetic time series of $AF^{GLB-RAW}$ and $AF^{GLB-ADJ}$ described above for each combination of start and end years. Positive slopes greater than 0.00025 yr^{-1} are shown as the light to dark red squares, slopes close to neutral are shown as the gray squares (slopes between -0.00025 and 0.00025 yr^{-1}), and negative slopes less than -0.00025 yr^{-1} are shown as the light to dark blue squares. Teal dots indicate trends that are statistically significant at the 1σ level and gold dots indicate trends that are statistically significant at the 2σ level. The statistical significance shown in Figures 4e and 4f is determined from the PDFs of

the 5000 synthetic $AF^{GLB-RAW}$ and $AF^{GLB-ADJ}$ time series for corresponding time frames, evaluated in a manner similar to the technique shown in Figures 4c and 4d.

If the $AF^{GLB-RAW}$ trend were truly positive, we would expect to see a majority of red squares in Figure 4e. However, the analysis shows that 43.7% of trends are positive, 18.8% are close to neutral, and 37.5% are negative. Examining Figure 4e from left to right reveals that most positive slopes with statistical significance at the 1σ level occur when the start year is earlier than 1965. Positive slopes with statistical significance at the 2σ level in this region of the figure have a start year prior to 1965 and an end year before 1990. Figure 4e shows that the majority of positive trends for $AF^{GLB-RAW}$ are associated with start years before 1965 and end years after the late 1980s. Nearly all prior published analyses of the trend in AF start in either 1959 or 1960. The analysis shown in Figure 4e demonstrates that the slope in $AF^{GLB-RAW}$ is quite sensitive to this early start of the data record. If the analysis is restricted to the 1970s through present, which covers approximately half a century, then the slopes in $AF^{GLB-RAW}$ tend to exhibit a near equal mixture between positive, neutral, and negative trends. The negative trends are dominated by start years in the late 1970s due to an unexplained anomaly in the CO_2 record from the South Pole and Mauna Loa time series. Some of these negative trends with start years in the late 1970s show statistical significance at the 1σ level. The strongest positive trends, showing statistical significance at the 2σ level, are associated with start years in the early 1990s due to the steep drawdown of atmospheric CO_2 following the eruption of Mount Pinatubo. All positive trends that are statistically significant at the 2σ level consider only 30–33 years of the 62-year data record and are restricted to either the first half or the last half of the data record.

Figure 4f shows that a majority of the slopes of $AF^{GLB-ADJ}$ are negative, regardless of the start and end year. This result is obtained because the adjustment for the influences of ENSO and volcanic eruptions removes a significant component of IAV from the data record. The largest population of negative slopes occurs when the start year is between 1970 and 1985 and the end year is between 2000 and 2021. Most of the $AF^{GLB-ADJ}$ trends that show statistical significance at the 1σ level occur during this period where the slopes are negative, with the exception of statistically significant positive trends at the 1σ level with start years in 1960 or earlier and end years around 1990, which only covers approximately the first half of the 62-year data record. Overall, about two-thirds of the mean slopes for $AF^{GLB-ADJ}$ are negative. The results shown in Figure 4d for $AF^{GLB-ADJ}$ show a nearly equal distribution between positive and negative slopes because this analysis considers the entire time period. Consequently, for the adjusted time series, the determination of the slope of the airborne fraction of CO_2 is somewhat dependent on whether the analysis begins at a time when the measurement of CO_2 began to be more global in nature (i.e., the early 1980s) or begins in a time period when the only available observations are from the South Pole and Mauna Loa.

3.2.2. Alternate Modeling Cases

Here we describe the AF trend analysis results, using raw and adjusted data, for the 10 alternate MLR modeling cases (Table 1) for comparison with results from our baseline simulation. Some of the alternate cases examine the CO_2 record only from Mauna Loa. Other alternate cases model the CO_2 growth rate at an annual or monthly time grid, using the N3.4 ENSO index, or various other SAOD records (Table 1 and Figures S5 through S14 in Supporting Information S1). We examine various MLR modeling cases that predict the CO_2 growth rate to determine if the alternative approaches and their adjustments to the CO_2 growth rate impact the scientific findings for the trends in AF from our baseline case.

Figure 5 shows the results of the airborne fraction trend analysis for each of these 11 cases. The MC analysis described in Section 2.3 is applied to $AF^{GLB-RAW}$, $AF^{GLB-ADJ}$, $AF^{MLO-RAW}$ and $AF^{MLO-ADJ}$ for each case. The colored dots and error bars in Figure 5a show the mean, 1σ, and 2σ standard deviation of the slopes for raw and adjusted data. Trends for all of the $AF^{GLB-RAW}$ (red dots) are identical, as the raw data are interpreted the same way following Equation 2. Similarly, trends for all of the $AF^{MLO-RAW}$ cases (yellow dots) are identical. For each case, the slopes found after adjusting for the influence of ENSO and major volcanic eruptions ($AF^{GLB-ADJ}$ and $AF^{MLO-ADJ}$) differ from one another. We show the $AF^{GLB-RAW}$ and $AF^{MLO-RAW}$ for all cases to provide a basis for comparison to the corresponding $AF^{GLB-ADJ}$ and $AF^{MLO-ADJ}$ values. Figure S17 in Supporting Information S1 shows results analogous to Figure 5, except the distributions are for Sen's slopes.

The $AF^{GLB-ADJ}$ and $AF^{MLO-ADJ}$ trends decrease in all cases, compared to $AF^{GLB-RAW}$ and $AF^{MLO-RAW}$, when accounting for the influence of natural variability on AF. The adjusted AF trends display a higher degree of variability compared to the raw AF trends among the 11 cases shown in Figure 5. $AF^{GLB-ADJ}$ ranges from
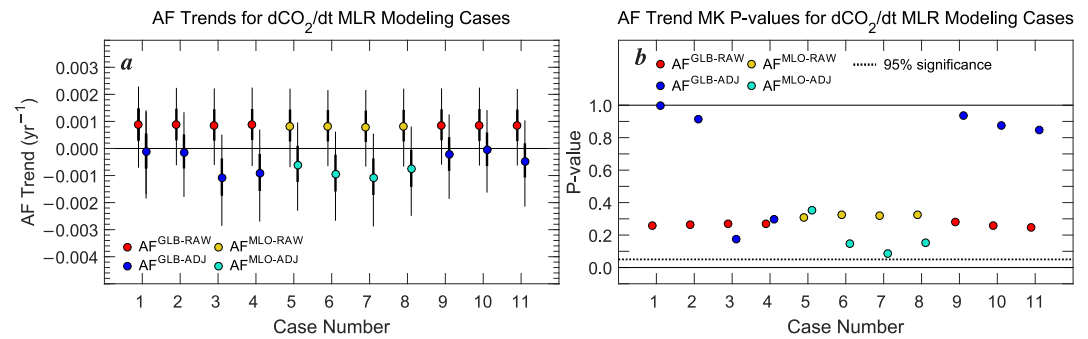
Figure 5. AF trend analysis for alternate MLR modeling cases as described in Table 1 in Section 2.2. (a) Trends in $AF^{GLB-RAW}$, $AF^{GLB-ADJ}$, $AF^{MLO-RAW}$, and $AF^{MLO-ADJ}$ for each case. Colored dots show the mean of slopes from the ordinary least squares linear regression of the 5000 synthetic AF time series attained from the MC simulations. Red dots show $AF^{GLB-RAW}$, blue dots show $AF^{GLB-ADJ}$, yellow dots show $AF^{MLO-RAW}$, and teal dots show $AF^{MLO-ADJ}$. Thick and thin black vertical lines show the 25th to 75th and 5th to 95th percentiles of the 5000 slopes. (b) Colored dots show the MK test P-values for the annual median AF time series for each raw and adjusted case.

-0.0011 ± 0.0010 yr^{-1} for case 3 that models the growth rate on an annual time grid with a CP and EP ENSO index, to -0.0001 ± 0.0010 yr^{-1} for case 1. Cases that examine $AF^{MLO-ADJ}$ trends are in a similar range as those of the $AF^{GLB-ADJ}$ trends. $AF^{MLO-ADJ}$ ranges from -0.0011 ± 0.0010 yr^{-1} for case 7 (similar to case 1 except the CO_2 growth rate is based only on data acquired at MLO and the MLR is conducted on an annual time grid) to -0.0006 ± 0.0010 yr^{-1} for case 5 (similar to case 1 except the CO_2 growth rate is based only on data acquired at MLO).

We examine the statistical significance of the AF trends by assessing the distribution of the 5000 synthetic raw and adjusted AF trends (Figure 5a) and the MK test P-values for the annual median raw and adjusted AF time series (Figure 5b). In all cases of Figure 5a, the thin vertical black lines representing the 5th to 95th percentile cross the 0.0 line, indicating that none of the trends in AF are statistically different from 0 at the 95% significance level. All of the MK P-values (Figure 5b) are greater than 0.05 (the 95% statistical significance threshold), again indicating that none of the trends in AF are statistically different from 0.

The results from our trend analysis when examining various cases continue to support the findings of Ballantyne et al. (2012, 2015) and Bennedsen et al. (2019) that the trend in $AF^{GLB-RAW}$ is positive, but not statistically different from 0 at the 2σ level. Furthermore, when the various MLR modeling approaches are used to adjust the CO_2 growth rate, our results are also in agreement again with studies by Knorr (2009) and Frölicher et al. (2013), discussed in the previous section. The trend in $AF^{GLB-ADJ}$ decreases when accounting for natural variability due to ENSO and volcanoes, but is also not statistically different from 0 at the 2σ level.

3.2.3. Alternate Land Use Change Emissions

Land use change CO_2 emissions are one of the most uncertain components of the global carbon cycle (Ballantyne et al., 2015; Friedlingstein et al., 2022). We repeat our analysis for the conditions of the baseline MLR model (case 1), except for various alternate estimates of land use change CO_2 emissions (E_{LUC}) to the atmosphere. Here, we consider 20 estimates of E_{LUC}, all from Friedlingstein et al. (2022): the three bookkeeping estimates, the 16 DGVMs, and an additional estimate which is the mean value of these 16 models (Section 2.1.2). We conduct the MC analysis for each of these 20 estimates of E_{LUC} (Figure S1 in Supporting Information S1). Additionally, we calculate AF trends determined from E_{FOS} only, without an estimate for E_{LUC} given the uncertainty around this quantity.

Figure 6 shows the trend analysis of $AF^{GLB-RAW}$ and $AF^{GLB-ADJ}$ for these 20 estimates of E_{LUC}. Results for the three bookkeeping methods and the 17 DGVM-based estimates of E_{LUC} appear in Figures 6a and 6b, respectively. In Figure 6c, $AF^{GLB-RAW}$ and $AF^{GLB-ADJ}$ have been calculated without an estimate for E_{LUC}. The red dots show the mean of the 5000 slopes from the MC analysis using the raw data ($AF^{GLB-RAW}$), whereas the blue dots show the mean of the 5000 slopes found following adjustment of the raw data using the specification for ENSO and SAOD of case 1 ($AF^{GLB-ADJ}$). The bookkeeping models and DGVMs used to estimate E_{LUC} are arranged on the x-axis in ascending order of the trend in $AF^{GLB-RAW}$. The raw and adjusted AF trends calculated using various
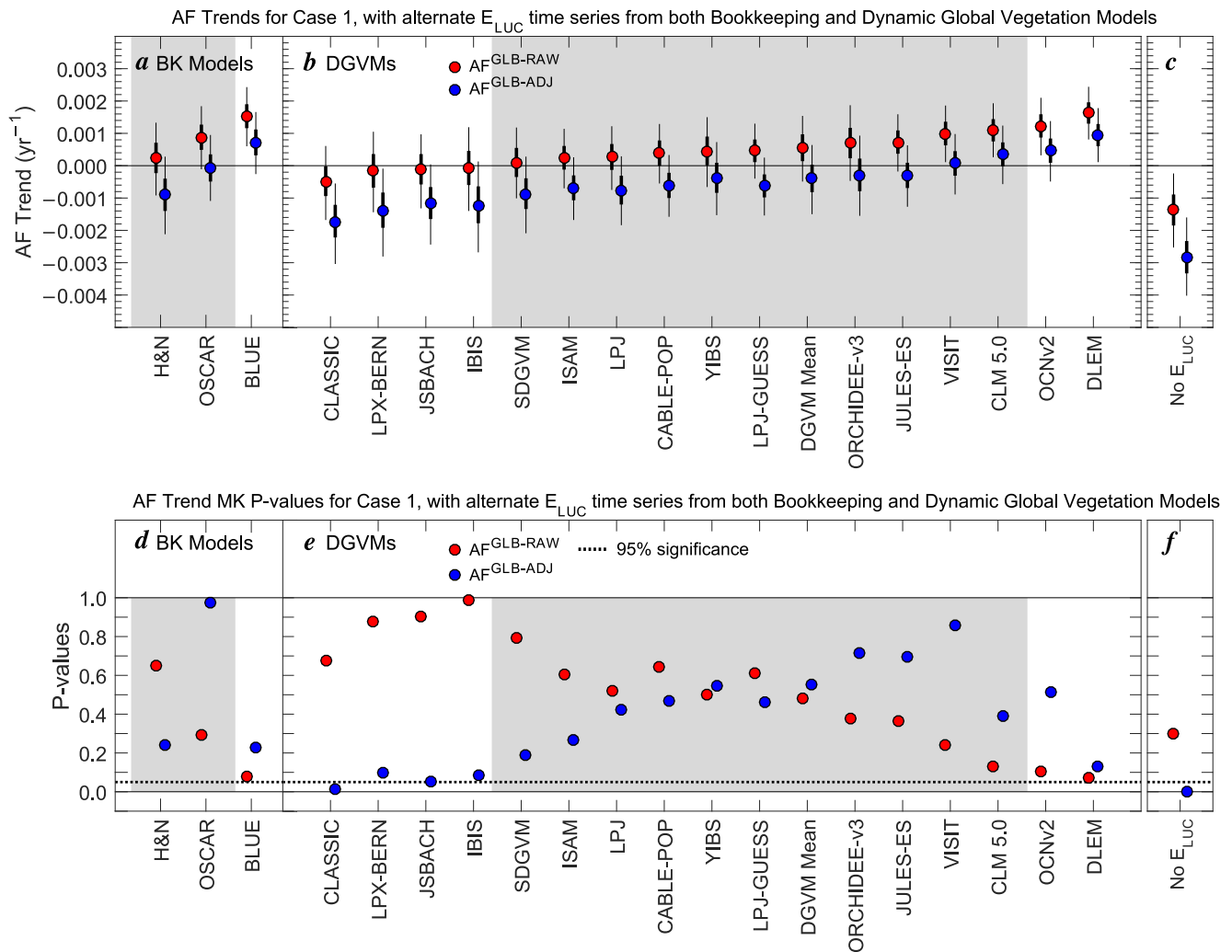
Figure 6. AF trends and their *P*-values for AF calculated using various estimates of E_{LUC}. (a) $AF^{GLB-RAW}$ and $AF^{GLB-ADJ}$ trends for each of the three bookkeeping models. Dots show the mean of the slopes from 5000 synthetic AF time series attained from the MC analysis. Red dots show $AF^{GLB-RAW}$, blue dots show $AF^{GLB-ADJ}$, and the thick and thin black vertical lines show the show 25th to 75th and 5th to 95th percentiles of the 5000 slopes. The vertical gray shading indicates models that fall within $\pm 1\sigma$ standard deviation about the mean of $AF^{GLB-RAW}$ slopes calculated from the three bookkeeping and 16 DGVM E_{LUC} estimates. (b) Same as (a) except for E_{LUC} from the 16 DGVMs and the multi-model mean. (c) Same as (a) except here AF is calculated without an estimate for E_{LUC}. (d) Colored dots show the MK test *P*-values for the annual median AF time series for each raw and adjusted case. (e) Same as (d) except for E_{LUC} from the 16 DGVMs and their multi-model mean. (f) Same as (d) except here AF is calculated without an estimate for E_{LUC}.

estimates of E_{LUC} (Figure 6) are more variable than the trends calculated using alternate MLR modeling cases to adjust the atmospheric CO_2 growth rate for a single, particular estimate of E_{LUC} (Figure 5). The gray shading on Figure 6 indicates the various computations of the slope of $AF^{GLB-RAW}$ that fall within the $\pm 1\sigma$ standard deviation about the mean of the slopes calculated from the three bookkeeping models and 16 DGVMs (the other DGVM-based estimate utilizes the multi-model mean, and is not considered for this uncertainty estimate). Figure S18 in Supporting Information S1 shows results analogous to Figure 6, except the distributions are for Sen's slopes.

We examine the statistical significance of the AF trends by assessing the distribution of the 5000 synthetic raw and adjusted AF time series (Figures 6a–6c) and the MK test P-values for the annual median raw and adjusted AF time series (Figures 6d–6f) for various estimates of E_{LUC}. The gray shaded region in Figures 6a and 6b indicates the E_{LUC} estimates that result in $AF^{GLB-RAW}$ trends that fall $\pm 1\sigma$ standard deviation of the mean $AF^{GLB-RAW}$ calculated from the three bookkeeping and 16 DGVM E_{LUC} estimates. In the gray shaded regions of Figures 6a and 6b, the thin vertical lines associated with 9 out of 11 $AF^{GLB-RAW}$ and all of the $AF^{GLB-ADJ}$ values cross the
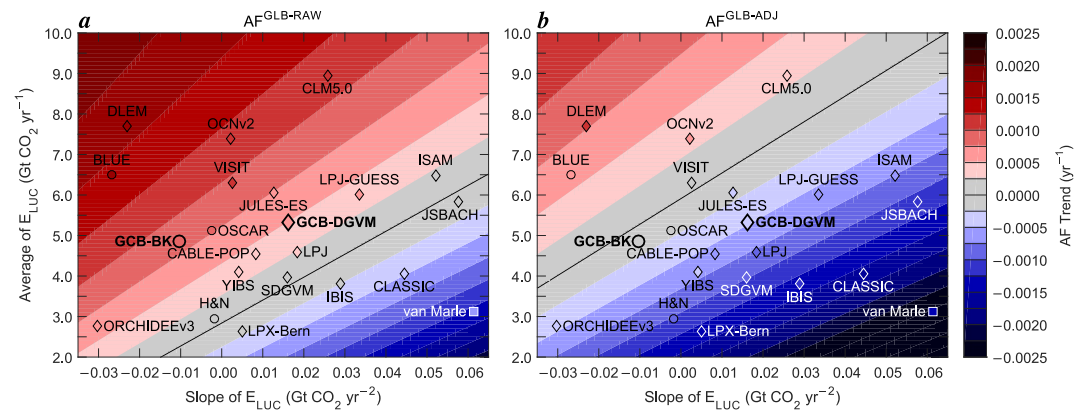
Figure 7. AF trend sensitivity to annual average E_{LUC} versus the slope of E_{LUC}. (a) $AF^{GLB-RAW}$ trend as a function of the annual average E_{LUC} (y-axis) and its slope (x-axis). (b) Same as (a) except for $AF^{GLB-ADJ}$. The black diagonal line represents an AF trend of 0. Negative AF slopes are shown in blue and positive AF slopes are shown in red. The AF trend for the average of the three bookkeeping models appears as the large circle labeled GCB-BK (i.e., case 1). Smaller circles show the AF trend for the individual bookkeeping models. The AF trend for the average of the 16 DGVMs appears as the large diamond labeled GCB-DGVM and small diamonds show the AF trend for individual DGVMs. The filled space inside each marker is colored by the magnitude of the AF trend reported in Figure 6. One additional square marker is shown on panels (a, b): the value of E_{LUC} and the slope of E_{LUC} from van Marle et al. (2022), filled using the color appropriate for their trend over the 1959 to 2019 time period.

0.0 line. This behavior indicates that these trends in AF are not statistically different from 0 at the 95% significance level. For the gray shaded regions of Figures 6d and 6e, all of the MK P-values are greater than 0.05 (the 95% statistical significance threshold), again indicating that these trends in AF are not statistically different from 0. The positive $AF^{GLB-RAW}$ trends determined from the BLUE bookkeeping model and the VISIT, CLM5.0, OCNv2, and DLEM DGVMs as well as the DLEM $AF^{GLB-ADJ}$ trend may be considered statistically significant at the 95% confidence level, as the vertical black lines do not cross the 0.0 line in Figures 6a and 6b. However, since the MK test P-values for all of the $AF^{GLB-RAW}$ time series are greater than 0.05, we conclude none of these trends differ from 0 at the 95% statistical significance threshold. The negative $AF^{GLB-ADJ}$ trend calculated using E_{LUC} from the CLASSIC DGVM is statistically significant at the 95% significance level on the basis of the vertical black line falling below the 0.0 line (Figure 6b) and an MK test P-value below 0.05 (Figure 6d). The trends in $AF^{GLB-ADJ}$ from the CLASSIC DGVM are outliers among all of the other trends shown in Figures 6b and 6e. Therefore, we conclude that trends in the airborne fraction of CO_2 are not statistically significant from 0 at the 95% confidence level for the vast majority of cases (20 out of 21) that account for various estimates of E_{LUC}, found using the time series adjusted for the effects of ENSO and major volcanic eruptions.

The analysis shown in Figures 6c and 6f is included as an illustrative example to show trends in AF calculated using E_{FOS} as the only anthropogenic emission source of CO_2. This calculation is similar to a case for AF trends considered by Ballantyne et al. (2012). Ignoring E_{LUC} results in a negative trend in $AF^{GLB-ADJ}$ of -0.0028 ± 0.0007 yr^{-1} that is statistically significant at the 95% significance level on the basis of the vertical black lines falling below 0 (Figure 6c) and on a MK test P-value less than 0.05 (Figure 6f). While at face value this result would be good news for the climate system, this approach is too simplistic because all estimates of E_{LUC} estimates are positive over our study period (Figure S1 in Supporting Information S1). A further narrowing of the effect of fossil fuel emissions on the airborne fraction of CO_2 without consideration of land use change could be accomplished by analyses of trends in carbon monoxide (CO) as well as ^{13}C (Bakwin et al., 1998) and ^{14}C (Basu et al., 2016, 2020; Siegenthaler & Oeschger, 1987) of atmospheric CO_2, since fossil fuel and land use change sources of carbon have different signatures on CO and the isotopic composition of CO_2.

Next, we analyze the sensitivity of the raw and adjusted AF trends to the E_{LUC} annual average and its slope, similar to framework used in the recently published analysis by van Marle et al. (2022). Figure 7 shows AF trends plotted as a function of the slope of E_{LUC} from 1959 to 2021 (x-axis) and mean value of E_{LUC} over this same time period (y-axis). The color bar used for AF is the result of a simple analysis that assumes a linear fit for E_{LUC} from 1959 to 2021, having a mean and slope corresponding to the values on the y-axis and x-axis, respectively. The resulting trends for the 21 estimates of E_{LUC} are displayed on Figure 7 at the corresponding mean and slope of the

actual data for each E_{LUC} time series. This analysis shows that as the annual average value of E_{LUC} increases, the trend in AF also rises. Conversely, as the slope of E_{LUC} increases, the trend in AF decreases. This simple analysis performs reasonably well at accounting for the trends in AF calculated from the 21 estimates of E_{LUC}, as shown by the tendency for the color-filled markers to match the background colors.

Our analysis of the sensitivity of the trends in AF to the mean and slope of E_{LUC} is consistent with the results of van Marle et al. (2022), as shown by the square marker on Figure 7. van Marle et al. (2022) concluded that the slope in the airborne fraction of CO_2 declined in a statistically significant manner over the 1959 to 2019 time period, upon adjustment for ENSO and major volcanic eruptions. This conclusion is based upon their independent estimate of E_{LUC}, that is not included in the GCB data set (Friedlingstein et al., 2022). The van Marle et al. estimate of the slope and annual mean magnitude of E_{LUC} is closest to the values of the slope and annual mean for E_{LUC} associated with the CLASSIC DGVM, shown in Figure 7. Details of the statistical analysis used by van Marle et al. (2022) were questioned by Bennedsen et al. (2023), leading to a retraction by van Marle et al. (2023) that acknowledges that their "statistical approach needs to be corrected." Since this retraction is based on criticism of their approach used to assess statistical significance, rather than their underlying time series of E_{LUC}, and since our use of their data involves only taking the mean and slope of their E_{LUC} time series, we have included the data from van Marle et al. (2022) on Figure 7. In this framework, the E_{LUC} time series of van Marle et al. (2022) is an outlier compared to all other estimates.

4. Comparison With Prior Studies

Our study examines the relative efficiency of the combined terrestrial biosphere and oceanic sinks by quantifying the trend of the airborne fraction (AF) of atmospheric CO_2 from 1959 to 2021. We show that the magnitude and in some cases the statistical significance of the trend in AF depends on whether the CO_2 growth rate is adjusted for the influence of ENSO and major volcanic eruptions. A statistically significant positive trend in AF would signify a change in the global carbon cycle to human-induced climate change that results in a greater relative abundance of CO_2 accumulating in the atmosphere, thereby enhancing the effects of global warming. Conversely, a statistically significant negative trend in AF would signify a change in the global carbon cycle to human-induced climate change that results in a decrease in the relative abundance of CO_2 accumulating in the atmosphere, signifying an enhancement in the strength of the terrestrial biosphere and oceanic carbon sinks.

Prior studies have reached varied conclusions regarding the sign and statistical significance of the trend in AF, as summarized in Table 2. These prior studies have examined trends in AF over a variety of time periods and have generally used a Monte Carlo (MC) analysis to assess statistical significance. In Table 2, we compare the results from this study to those of previous analyses over the same time period used in the prior publication. All of the studies summarized in Table 2 that adjust the CO_2 growth rate have used a single ENSO index (either the N3, N3.4, Multivariate ENSO Index, or the Southern Oscillation Index (SOI)) to adjust for conditions in the Tropical Pacific and the Volcanic Aerosol Index (VAI) from Ammann et al. (2003a, 2003b) as the basis for the volcanic adjustment to the CO_2 growth rate, with the exception of Frölicher et al. (2013) that used a volcanic adjustment from an Earth System Model. For the trends denoted "this study" in Table 2, we use a time series for SAOD over land based on data prepared for CMIP6 GCM simulations (1959–1978) and the GloSSAC v2.2 data record (1979–2021) and ENSO indices representing conditions in both the Central and Eastern Tropical Pacific, in order to be consistent with the baseline simulation highlighted throughout Section 3. Results for AF trend from "this study" are given with the same units as the prior publication. The prior studies have also used various data sources for E_{FOS} and E_{LUC} (Equation 1) as well as atmospheric CO_2 (the basis of dCO_2/dt).

First we describe studies that find AF has risen with statistical significance over time. Canadell et al. (2007) used the SOI and VAI indices to determine the contribution of natural variability to the airborne fraction of CO_2 from ENSO and volcanic activity. They removed the effects along with any other high frequency component of AF via a monthly "reduced noise" approach. The statistical significance of the trends in AF was tested using an MC analysis coupled with a first-order autoregressive (AR) model to generate synthetic time series. The MC analysis was applied to the AF time series alone and not to each component used to compute AF. Canadell et al. (2007) concluded that AF had risen at a rate of $0.25 \pm 0.21\%$ yr^{-1} from 1959 to 2006 with a statistical significance at the 89% level. They also noted this rise in AF was faster than expected, based on an analysis of output from 11 climate models. Most importantly, Canadell et al. (2007) report "nearly identical proportional trends in AF" with and without an adjustment for the influence of ENSO and major volcanic eruptions. Conversely, our AF trend for

Table 2
Trends in AF From Prior Research Compared to Trends From This Study

Analysis	Study period	ENSO & volcanic adjusted	AF trend prior study	Statistically significant	$AF^{GLB-RAW}$ trend this study	$AF^{GLB-ADJ}$ trend this study	Statistically significant
Canadell et al. (2007)	1959–2006	Yes	$0.25 \pm 0.21\%$ yr^{-1}	Yes (89%)	$0.18 \pm 0.19\%$ yr^{-1}	$0.07 \pm 0.19\%$ yr^{-1}	No
Raupach et al. (2008)	1959–2006	Yes	$0.24 \pm 0.14\%$ yr^{-1}	Yes (92%)	$0.18 \pm 0.19\%$ yr^{-1}	$0.07 \pm 0.19\%$ yr^{-1}	No
Le Quéré et al. (2009)	1959–2008	Yes	$0.30 \pm 0.20\%$ yr^{-1}	Yes (90%)	$0.15 \pm 0.18\%$ yr^{-1}	$0.06 \pm 0.18\%$ yr^{-1}	No
Raupach et al. (2014)	1959–2013	Yes	$0.24 \pm 0.20\%$ yr^{-1}	Yes (89%)	$0.10 \pm 0.16\%$ yr^{-1}	$0.01 \pm 0.16\%$ yr^{-1}	No
Knorr (2009)	1959–2007	Yes	$-0.02 \pm 0.17\%$ yr^{-1}	No	$0.18 \pm 0.18\%$ yr^{-1}	$0.06 \pm 0.19\%$ yr^{-1}	No
Frölicher et al. (2013)	1960–2009	Yes	$-0.17 \pm 0.07\%$ yr^{-1}	No	$0.13 \pm 0.18\%$ yr^{-1}	$0.02 \pm 0.18\%$ yr^{-1}	No
Ballantyne et al. (2012)	1959–2010	No	0.0012 ± 0.0010 yr^{-1}	No	0.0009 ± 0.0012 yr^{-1}	0.0002 ± 0.0013 yr^{-1}	No
Bennedsen et al. (2019)	1959–2016	No	0.0011 ± 0.0018 yr^{-1}	No	0.0010 ± 0.0010 yr^{-1}	0.0000 ± 0.0011 yr^{-1}	No

Note. The study period of each prior analysis, whether or not the growth rate of CO_2 or AF was adjusted for the influence of ENSO and major volcanic eruptions in the prior analysis, the AF trend from the prior study, and whether the prior study reported statistical significance for the trend in AF. If statistical significance was reported, the level of significance is given within parentheses. Trends in AF found from this study for the baseline case of Section 3, for the raw CO_2 growth rate ($AF^{GLB-RAW}$) and for the growth rate adjusted for ENSO and major volcanoes ($AF^{GLB-ADJ}$) are shown for the time period of the prior study, in the units as the prior study. The uncertainty for AF trends from prior studies and this study are shown at the $\pm 1\sigma$ level.

1959 to 2006 is $0.18 \pm 0.19\%$ yr^{-1} without such an adjustment, which is more than twice the value of $0.07 \pm 0.19\%$ yr^{-1} found using the adjusted time series for dCO_2/dt. Therefore, the difference between our conclusion of little to no rise in the AF of CO_2 over the 1959 to 2006 time period, compared to the conclusion of Canadell et al. (2007) that AF had risen in a statistically significant manner at the 89% confidence level, is likely due to differences in how the adjustments for ENSO and volcanoes have been implemented.

The studies of Raupach et al. (2008), Le Quéré et al. (2009), and Raupach et al. (2014) (hereafter RLQR) all report a statistically significant rise in the AF of CO_2 over various time periods (Table 2). These three studies were conducted by many of the same persons as the Canadell et al. (2007) study, and a similar methodology was used to adjust dCO_2/dt in all of these studies. As for the comparison of our AF trend values to those from Canadell et al. (2007), we find better agreement with the values for the AF trends of RLQR (i.e., $0.18 \pm 0.19\%$ yr^{-1}, $0.15 \pm 0.18\%$ yr^{-1}, and $0.10 \pm 0.16\%$ yr^{-1} for time periods of 1959–2006, 1959 to 2008, and 1959 to 2013, respectively) using $AF^{GLB-RAW}$ rather than the values found using $AF^{GLB-ADJ}$ shown in Table 2.

Two other studies shown in Table 2 have accounted for natural variability when analyzing the trend in the AF of atmospheric CO_2 (Frölicher et al., 2013; Knorr, 2009). Each of these studies show that the trend in AF may be negative (Table 2). We find a similar estimate for the AF trend over 1959 to 2007 reported by Knorr (2009) (their $-0.02 \pm 0.17\%$ yr^{-1} compared to our $0.06 \pm 0.19\%$ yr^{-1}). Similar to Knorr (2009), we conclude these small trends are not statistically significant. Most interestingly, Knorr (2009) used the N3 index and VAI to account for ENSO and volcanic influences on dCO_2/dt, which are the same parameters used by Raupach et al. (2008, 2014) for the 1959 to 2006 and 1959 to 2013 periods, respectively. The similarity of our trend with that of Knorr (2009), and the difference of our trend reported in the two Raupach et al. (2008, 2014) studies, underscores that the likely root cause of the difference between our conclusions compared to those of RLQR is likely due to the methodology used to adjust for the influence of natural variability on dCO_2/dt.

Frölicher et al. (2013) quantify the effect of volcanic eruptions on dCO_2/dt using the NCAR CSM1.4-carbon model. They report a longer impact of volcanic eruptions on the global carbon cycle than one would find using a linear assumption between aerosol index data (i.e., such as our SAOD) and dCO_2/dt. Frölicher et al. (2013) report a decline in AF of $-0.17 \pm 0.07\%$ yr^{-1} over 1960–2009, whereas we find a slight rise of $0.02 \pm 0.18\%$ yr^{-1}. Neither of these trends are statistically significant at the 1σ (68%) level. Nonetheless, if the approach adopted by Frölicher et al. (2013) to adjust for volcanic influence is more realistic than the method used here as well as in most other prior studies, this would be good news for Earth's climate system because the negative AF trend reported by Frölicher et al. implies there might be feedbacks in the coupled climate—carbon cycle system that lead to more effective sequestration of anthropogenic CO_2 over time. It is also possible that differences between

AF trends reported in prior studies and those found using our baseline case are due to differences in emissions of CO_2 due to land use change, given the sensitivity of trends in $AF^{GLB-RAW}$ and $AF^{GLB-ADJ}$ to E_{LUC} shown in Figures 6 and 7. It is beyond the scope of this analysis to re-compute trends in $AF^{GLB-RAW}$ and $AF^{GLB-ADJ}$ using the original values of E_{LUC} from the prior studies, given the lack of data archiving associated with prior publications.

Ballantyne et al. (2012) and Bennedsen et al. (2019) reported AF trends without adjusting for the influence of ENSO and major volcanic eruptions. Our values for the trends in $AF^{GLB-RAW}$ given in Table 2 are in close quantitative agreement with values reported by both of these prior studies. Similarly, we all find no statistical significance to these trends at the 1σ level. Bennedsen et al. (2019) used an estimate for E_{LUC} similar to that of our baseline case, albeit from an earlier GCB report. Ballantyne et al. (2012) incorporated three independent estimates for E_{LUC} in a Monte Carlo framework. Given the importance of the adjustment for natural variability on the AF trend, we shall not provide further details of these two prior studies.

5. Conclusions

We analyze the growth rate of atmospheric CO_2 from 1959 to 2021 using a multiple linear regression (MLR) model that includes time series that represent anthropogenic emissions of CO_2 from the combustion of fossil fuels, cement production, and land use change, as well as the strength of El Niño-Southern Oscillation (ENSO) events and major volcanic eruptions. Output from the MLR model is used to adjust the growth rate of atmospheric CO_2 for natural variability due to ENSO and volcanoes. Trends in the airborne fraction of atmospheric CO_2 are quantified using data representing both the observed raw and adjusted global atmospheric CO_2 growth rate ($d CO_2/dt$). The MLR model accounts for approximately 77% of the observed inter-annual variability in the global atmospheric CO_2 growth rate.

The first critical component of our study is evaluation of trends in the airborne fraction atmospheric of CO_2 (AF) using a raw time series for $d CO_2/dt$ (termed $AF^{GLB-RAW}$) and an adjustment of $d CO_2/dt$ for natural variability arising from ENSO and major volcanic eruptions (termed $AF^{GLB-ADJ}$). The adjustment of $d CO_2/dt$ for natural variability is essential because most of the significant El Niño events that increase $d CO_2/dt$ occurred in the last four decades of the 1959 to 2021 study period, whereas all of the major volcanic activity that decrease $d CO_2/dt$ occurred in the first four decades. The second critical component of our study is evaluation of trends in AF for numerous time series of the emission of CO_2 due to land use change (E_{LUC}), which we obtained from the 2022 Global Carbon Budget (GCB) report (Friedlingstein et al., 2022). The third critical component of our study is the quantitative evaluation of the uncertainty of trends in $AF^{GLB-RAW}$ and $AF^{GLB-ADJ}$ using 5000 member, auto-regressive Monte Carlo analysis, based on the approach of Ballantyne et al. (2012, 2015). Finally, we also quantify trends and uncertainty in $AF^{GLB-RAW}$ and $AF^{GLB-ADJ}$ for various start and end years, facilitating the comparison to prior published analyses and allowing for the robustness of trends for the entire 1959 to 2021 time period to be assessed.

The baseline simulation of $AF^{GLB-RAW}$ and $AF^{GLB-ADJ}$ uses indices for ENSO conditions in the CP and EP and E_{LUC} based on the average of the three bookkeeping-model time series published by GBC 2022. For the 1959 to 2021 time period, the trend in $AF^{GLB-RAW}$ is 0.0009 ± 0.0009 yr^{-1} and the trend in $AF^{GLB-ADJ}$ is -0.0001 ± 0.0010 yr^{-1}, with a Sen's slope of 0.0011 ± 0.0009 yr^{-1} and 0.0001 ± 0.0006 yr^{-1}. Neither trend differs from 0 with statistical significance at the 2σ (95%) level based upon the Mann-Kendall test P-values, as well as the probability distribution of trends found from the MC analysis. There are certain combinations of start and end years that yield increases in AF that are statistically significant at the 2σ level, but the vast majority of these pockets of statistical significance are associated with $AF^{GLB-RAW}$ rather than $AF^{GLB-ADJ}$ (Figure 4). Consequently, upon adjustment for the influence of natural variability and use of the mean of the three GCB 2022 bookkeeping estimates for E_{LUC}, it is extremely likely that the relative efficiency of the combined global terrestrial biosphere and oceanic carbon sinks has been constant relative to anthropogenic emissions over the past six decades.

The most important component in the uncertainty of trends in both $AF^{GLB-RAW}$ and $AF^{GLB-ADJ}$ is the specification of the global, annual emission of CO_2 due to land use change (E_{LUC}). Therefore, we quantified AF trends for each of the three bookkeeping estimates for E_{LUC} published by GCB 2022, as well as the 16 time series for E_{LUC} from various Dynamic Global Vegetative Models (DGVMs) (Figure 6). There is considerable spread in the trend of both $AF^{GLB-RAW}$ and $AF^{GLB-ADJ}$ for the various E_{LUC} estimates. This spread highlights one of the most

important conclusions of our study: more precise knowledge of the actual value of the trend in the airborne fraction of atmospheric CO_2 requires resolving the current large differences in various estimates of E_{LUC}. For all cases the trend in $AF^{GLB-RAW}$ exceeds that of $AF^{GLB-ADJ}$, further highlighting the importance of the adjustment of dCO_2/dt for natural variability (Figure 6). None of the trends in $AF^{GLB-RAW}$ are statistically significant from 0 at the 95% confidence level, whereas one of the trends in $AF^{GLB-ADJ}$ (for the CLASSIC DGVM) exhibits a statistically significant decline over the 1959 to 2021 time period. Since the value of E_{LUC} from the CLASSIC DGVM is an outlier compared to the other E_{LUC} estimates (Figures 6 and 7), the overall analysis leads us to conclude it is very likely that the relative efficiency of the combined global terrestrial biosphere and oceanic carbon sinks has been fairly constant on a global scale over the past six decades.

Data Availability Statement

The global atmospheric CO_2 data was downloaded from NOAA Earth System Research Laboratories (ESRL) at https://gml.noaa.gov/ccgg/trends/gl_data.html (Lan & Thoning, 2023), the atmospheric CO_2 data observed at Mauna Loa, Hawaii was downloaded from NOAA ESRL at https://gml.noaa.gov/ccgg/trends/data.html (Tans & NOAA/GML, 2023; Keeling & Scripps Institution of Oceanography, 2023), and the atmospheric CO_2 observed at the South Pole was downloaded from the Scripps CO_2 Program at https://scrippsco2.ucsd.edu/data/atmospheric_co2/spo.html (Keeling & Scripps Institution of Oceanography, 2023). All anthropogenic CO_2 emissions data were obtained from the "2022 Global Budget 2022 v1.0" file downloaded from https://www.icos-cp.eu/science-and-impact/global-carbon-budget/2022 (Global Carbon Project, 2022). A description of the Volcanic Forcing data set for CMIP6 GCMs can be found at https://docs.google.com/document/d/1pU9IiJvPJwRvIgVaSDdJ4O0Jeorv_2ekEtted34K9cA/edit#heading=h.jdoykiw7tpen (Durack & Taylor, 2022); the actual stratospheric extinction coefficient data set used in our analysis is the CMIP_1850_2014_extinction_550nm_strat_only_v3. nc file available at https://arggit.usask.ca/cj/eva-data-hub/-/tree/main/data (University of Saskatchewan) (Ogilvie & Toohey, 2022) and https://doi.org/10.5281/zenodo.10392761 (Bennett, 2023). The GloSSAC v2.2 data set was downloaded from https://opendap.larc.nasa.gov/opendap/GloSSAC/GloSSAC_2.2/contents.html (Thomason et al., 2022). The Volcanic Aerosol Index of Ammann et al. (2003a, 2003b) was downloaded from NOAA National Centers for Environmental Information at https://www.ncei.noaa.gov/access/paleo-search/ by searching for the Ammann et al. (2003a, 2003b) Monthly Volcanic Forcing Data for Climate Modeling 1890–1999 data set. The Stratospheric Aerosol Optical Depth data set of Sato et al. (1993) was downloaded from https://data.giss.nasa.gov/modelforce/strataer/ (Sato et al., 2016). All ENSO indices (Reynolds et al., 2002) were downloaded from the NOAA National Centers for Environmental Prediction Climate Prediction Center at https://www.cpc.ncep.noaa.gov/data/indices/ (NOAA/CPC, 2023). Finally, the Matlab code and data files used in the analysis and to produce related figures is available at https://doi.org/10.5281/zenodo.10392761 (Bennett, 2023).

References

Ammann, C. M., Meehl, G. A., Washington, W. M., & Zender, C. S. (2003a). A monthly and latitudinally varying volcanic forcing dataset in simulations of 20th century climate. *Geophysical Research Letters*, *30*(12), 1–4. https://doi.org/10.1029/2003GL016875

Ammann, C. M., Meehl, G. A., Washington, W. M., & Zender, C. S. (2003b). Monthly volcanic forcing data for climate modeling 1890-1999. [Dataset]. NOAA. https://doi.org/10.25921/ts5e-aw60

Anderegg, W. R. L., Ballantyne, A. P., Smith, W. K., Majkut, J., Rabin, S., Beaulieu, C., et al. (2015). Tropical nighttime warming as a dominant driver of variability in the terrestrial carbon sink. *Proceedings of the National Academy of Sciences of the United States of America*, *112*(51), 15591–15596. https://doi.org/10.1073/pnas.1521479112

Arfeuille, F., Weisenstein, D., MacK, H., Rozanov, E., Peter, T., & Brönnimann, S. (2014). Volcanic forcing for climate modeling: A new microphysics-based data set covering years 1600-present. *Climate of the Past*, *10*(1), 359–375. https://doi.org/10.5194/cp-10-359-2014

Bakwin, P. S., Tans, P. P., Andres, J., & Conway, C. O. (1998). Determination of the isotopic (^{13}C/^{12}C) discrimination of atmospheric. *Global Biogeochemical Cycles*, *12*(3), 555–562. https://doi.org/10.1029/98GB02265

Ballantyne, A. P., Alden, C. B., Miller, J. B., Trans, P. P., & White, J. W. C. (2012). Increase in observed net carbon dioxide uptake by land and oceans during the past 50 years. *Nature*, *488*(7409), 70–73. https://doi.org/10.1038/nature11299

Ballantyne, A. P., Andres, R., Houghton, R., Stocker, B. D., Wanninkhof, R., Anderegg, W., et al. (2015). Audit of the global carbon budget: Estimate errors and their impact on uptake uncertainty. *Biogeosciences*, *12*(8), 2565–2584. https://doi.org/10.5194/bg-12-2565-2015

Basu, S., Lehman, S. J., Miller, J. B., Andrews, A. E., Sweeney, C., Gurney, K. R., et al. (2020). Estimating US fossil fuel CO_2 emissions from measurements of ^{14}C in atmospheric CO_2. *Proceedings of the National Academy of Sciences of the United States of America*, *117*(24), 13300–13307. https://doi.org/10.1073/pnas.1919032117

Basu, S., Miller, J. B., & Lehman, S. (2016). Separation of biospheric and fossil fuel fluxes of CO_2 by atmospheric inversion of CO_2 and $^{14}CO_2$ measurements: Observation System Simulations. *Atmospheric Chemistry and Physics*, *16*(9), 5665–5683. https://doi.org/10.5194/acp-16-5665-2016

Bennedsen, M., Hillebrand, E., & Jan Koopman, S. (2019). Trend analysis of the airborne fraction and sink rate of anthropogenically released CO_2. *Biogeosciences*, *16*(18), 3651–3663. https://doi.org/10.5194/bg-16-3651-2019

Bennedsen, M., Hillebrand, E., & Koopman, S. J. (2023). On the evidence of a trend in the CO_2 airborne fraction. *Nature*, *616*(7956), E1–E3. https://doi.org/10.1038/s41586-023-05871-6

Bennett, B. F. (2023). Quantification of the trends in the airborne fraction of atmospheric CO_2 [Software] [Dataset]. Zenodo. https://doi.org/10.5281/zenodo.10392761

Betts, R. A., Jones, C. D., Knight, J. R., Keeling, R. F., & Kennedy, J. J. (2016). El Niño and a record CO_2 rise. *Nature Climate Change*, *6*(9), 806–810. https://doi.org/10.1038/nclimate3063

Bradley, R. S., Diaz, H. F., Kiladis, G. N., & Eischeid, J. K. (1987). ENSO signal in continental temperature and precipitation records. *Nature*, *327*(6122), 497–501. https://doi.org/10.1038/327497a0

Brum, M., López, J. G., Asbjornsen, H., Licata, J., Pypker, T., Sanchez, G., & Oiveira, R. S. (2018). ENSO effects on the transpiration of eastern Amazon trees. *Philosophical Transactions of the Royal Society B: Biological Sciences*, *373*(1760), 20180085. https://doi.org/10.1098/rstb.2018.0085

Canadell, J. G., Le Quéré, C., Raupach, M. R., Field, C. B., Buitenhuis, E. T., Ciais, P., et al. (2007). Contributions to accelerating atmospheric CO_2 growth from economic activity, carbon intensity, and efficiency of natural sinks. *Proceedings of the National Academy of Sciences of the United States of America*, *104*(47), 18866–18870. https://doi.org/10.1073/pnas.0702737104

Canadell, J. G., Monteiro, P. M., Costa, M. H., Syampungani, S., Zaehle, S., Zickfeld Canada, K., & Alexandrov, G. A. (2021). *SPM 673 5 global carbon and other biogeochemical cycles and feedbacks coordinating lead authors: Lead authors: Contributing authors*. IPCC. https://doi.org/10.1017/9781009157896.007.674

Cao, Z., Myers, R. J., Lupton, R. C., Duan, H., Sacchi, R., Zhou, N., et al. (2020). The sponge effect and carbon emission mitigation potentials of the global cement cycle. *Nature Communications*, *11*(1), 1–9. https://doi.org/10.1038/s41467-020-17583-w

Cavaleri, M. A., Coble, A. P., Ryan, M. G., Bauerle, W. L., Loescher, H. W., & Oberbauer, S. F. (2017). Tropical rainforest carbon sink declines during El Niño as a result of reduced photosynthesis and increased respiration rates. *New Phytologist*, *216*(1), 136–149. https://doi.org/10.1111/nph.14724

Chatterjee, A., Gierach, M. M., Sutton, A. J., Feely, R. A., Crisp, D., Eldering, A., et al. (2017). Influence of El Niño on atmospheric CO_2 over the tropical Pacific Ocean: Findings from NASA's OCO-2 mission. *Science*, *358*(6360). https://doi.org/10.1126/science.aam5776

Chylek, P., Tans, P., Christy, J., & Dubey, M. K. (2018). The carbon cycle response to two El Niño types: An observational study. *Environmental Research Letters*, *13*(2), 024001. https://doi.org/10.1088/1748-9326/aa9c5b

Conway, T. J., Tans, P. P., Waterman, L. S., Thoning, K. W., Kitzis, D. R., Masarie, K. A., & Zhang, N. (1994). Evidence for interannual variability of the carbon cycle from the national oceanic and atmospheric administration/climate monitoring and diagnostics Laboratory Global Air Sampling Network. *Journal of Geophysical Research*, *99*(D11), 22831–22855. https://doi.org/10.1029/94jd01951

Cox, P. M., Betts, R. A., Jones, C. D., Spall, S. A., & Totterdell, I. J. (2000). Acceleration of global warming due to carbon-cycle feedbacks in a coupled climate model. *Nature*, *408*(6809), 184–187. https://doi.org/10.1038/35041539

Denters, B., & Van Pruijenbroek, R. A. G. (1989). Multivariate analysis Problems, solutions and an application. *Quality and Quantity*, *108*, 83–108. https://doi.org/10.1007/BF00195408

DeVries, T., Holzer, M., & Primeau, F. (2017). Recent increase in oceanic carbon uptake driven by weaker upper-ocean overturning. *Nature*, *542*(7640), 215–218. https://doi.org/10.1038/nature21068

Durack, P., & Taylor, K. (2022). CMIP6 forcing datasets summary (version 6.2.43). Retrieved from https://docs.google.com/document/d/1pU9IiJvPJwRvIgVaSDdJ4O0Jeorv_2ekEtted34K9cA/edit#heading=h.jdoykiw7tpen

Dutton, E. G., & Christy, J. R. (1992). Solar radiative forcing at selected locations and evidence for global lower tropospheric cooling following the eruptions of El Chichón and Pinatubo. *Geophysical Research Letters*, *19*(23), 2313–2316. https://doi.org/10.1029/92GL02495

Dutton, E. G., & Bodhaine, B. A. (2001). Solar irradiance anomalies caused by clear-sky transmission variations above Mauna Loa: 1958-1999. *Journal of Climate*, *14*(15), 3255–3262. https://doi.org/10.1175/1520-0442(2001)014<3255:SIACBC>2.0.CO;2

Dyer, A. J., & Hicks, B. B. (1968). Global spread of volcanic dust from the Bali eruption of 1963, 545–554. https://doi.org/10.1002/qj.49709440209

Fan, Y., & van den Dool, H. (2008). A global monthly land surface air temperature analysis for 1948-present. *Journal of Geophysical Research*, *113*(1), 1–18. https://doi.org/10.1029/2007JD008470

Fay, A. R., Gregor, L., Landschützer, P., Mckinley, G. A., Gruber, N., Iida, Y., et al. (2021). Harmonization of global surface ocean pCO2 mapped products and their flux calculations; an improved estimate of the ocean carbon sink. *Earth System Science Data*, (March), 1–32. https://doi.org/10.5194/essd-2021-16

Forkel, M., Carvalhais, N., Rödenbeck, C., Keeling, R., Heimann, M., Thonicke, K., et al. (2016). Enhanced seasonal CO_2 exchange caused by amplified plant productivity in northern ecosystems. *Science*, *351*(6274), 696–699. https://doi.org/10.1126/science.aac4971

Friedlingstein, P., Fung, I., Holland, E., John, J., Brasseur, G., Erickson, D., & Schimel, D. (1995). On the contribution of CO_2 fertilization to the missing biospheric sink. *Global Biogeochemical Cycles*, *9*(4), 541–556. https://doi.org/10.1029/95GB02381

Friedlingstein, P., O'Sullivan, M., Jones, M. W., Andrew, R. M., Hauck, J., Olsen, A., et al. (2020). Global carbon budget 2020. *Earth System Science Data*, *12*(4), 3269–3340. https://doi.org/10.5194/essd-12-3269-2020

Friedlingstein, P., Sullivan, M. O., Jones, M. W., Andrew, R. M., Gregor, L., Hauck, J., et al. (2022). Global carbon budget. *Earth System Science Data*, *14*(11), 4811–4900. https://doi.org/10.5194/essd-14-4811-2022

Frölicher, T. L., Joos, F., Raible, C. C., & Sarmiento, J. L. (2013). Atmospheric CO_2 response to volcanic eruptions: The role of ENSO, season, and variability. *Global Biogeochemical Cycles*, *27*(1), 239–251. https://doi.org/10.1002/gbc.20028

Fuller, D. O., & Murphy, K. (2006). The ENSO-fire dynamic in insular Southeast Asia. *Climatic Change*, *74*(4), 435–455. https://doi.org/10.1007/s10584-006-0432-5

Gao, C., Robock, A., & Ammann, C. (2008). Volcanic forcing of climate over the past 1500 years: An improved ice core-based index for climate models. *Journal of Geophysical Research*, *113*(23), 1–15. https://doi.org/10.1029/2008JD010239

Gasser, T., Crepin, L., Quilcaille, Y., Houghton, R. A., Ciais, P., & Obersteiner, M. (2020). Historical CO_2 emissions from land use and land cover change and their uncertainty. *Biogeosciences*, *17*(15), 4075–4101. https://doi.org/10.5194/bg-17-4075-2020

Global Carbon Project. (2022). Supplemental data of global carbon budget 2022 (version 1.0) [Dataset]. Global Carbon Project. https://doi.org/10.18160/gcp-2022

Graham, R. L., Turner, M. G., Dale, V. H., Graham, R. L., Monica, G., & Dale, V. H. (1990). How increasing CO_2 and climate change affect forests. *BioScience*, *40*(8), 575–587. https://doi.org/10.2307/1311298

Grossiord, C., Buckley, T. N., Cernusak, L. A., Novick, K. A., Poulter, B., Siegwolf, R. T. W., et al. (2020). Plant responses to rising vapor pressure deficit. *New Phytologist*, *226*(6), 1550–1566. https://doi.org/10.1111/nph.16485

Gu, L., Baldocchi, D. D., Wofsy, S. C., William Munger, J., Michalsky, J. J., Urbanski, S. P., & Boden, T. A. (2003). Response of a deciduous forest to the Mount Pinatubo eruption: Enhanced photosynthesis. *Science*, *299*(5615), 2035–2038. https://doi.org/10.1126/science.1078366

Guo, R., Wang, J., Bing, L., Tong, D., Ciais, P., Davis, S. J., et al. (2021). Global CO_2 uptake by cement from 1930 to 2019. *Earth System Science Data*, *13*(4), 1791–1805. https://doi.org/10.5194/essd-13-1791-2021

Gurney, K. R., Castillo, K., Li, B., & Zhang, X. (2012). A positive carbon feedback to ENSO and volcanic aerosols in the tropical terrestrial biosphere. *Global Biogeochemical Cycles*, *26*(1), 1–9. https://doi.org/10.1029/2011GB004129

Hansis, E., Davis, S. J., & Pongratz, J. (2015). Relevance of methodological choices for accounting of land use change carbon fluxes. *Global Biogeochemical Cycles*, *29*(8), 1230–1246. https://doi.org/10.1002/2014GB004997

Houghton, R. A., & Nassikas, A. A. (2017). Global and regional fluxes of carbon from land use and land cover change 1850-2015. *Global Biogeochemical Cycles*, *31*(3), 456–472. https://doi.org/10.1111/1462-2920.13280

Huang, B., Thorne, P. W., Banzon, V. F., Boyer, T., Chepurin, G., Lawrimore, J. H., et al. (2017). Extended reconstructed Sea surface temperature, Version 5 (ERSSTv5): Upgrades, validations, and intercomparisons. *Journal of Climate*, *30*(20), 8179–8205. https://doi.org/10.1175/JCLI-D-16-0836.1

Huang, M. T., & Zhai, P. M. (2021). Achieving Paris Agreement temperature goals requires carbon neutrality by middle century with far-reaching transitions in the whole society. *Advances in Climate Change Research*, *12*(2), 281–286. https://doi.org/10.1016/j.accre.2021.03.004

IPCC. (2021). In *Climate change 2021: The physical science basis. Contribution of working group I to the sixth assessment report of the intergovernmental panel on climate change.* https://doi.org/10.1017/9781009157896

Jones, C. D., & Cox, P. M. (2005). On the significance of atmospheric CO_2 growth rate anomalies in 2002-2003. *Geophysical Research Letters*, *32*(14), 1–4. https://doi.org/10.1029/2005GL023027

Jones, C. D., & Cox, P. M. (2001). Modeling the volcanic signal in the atmospheric CO_2 record. *Global Biogeochemical Cycles*, *15*(2), 453–465. https://doi.org/10.1029/2000GB001281

Keeling, C. D., Bacastow, R. B., Bainbridge, A. E., Ekdahl, C. A., Guenther, P. R., Waterman, L. S., & Chin, J. F. S. (1976). Atmospheric carbon dioxide variations at Mauna Loa Observatory, Hawaii. *Tellus*, *28*(6), 538–551. https://doi.org/10.3402/tellusa.v28i6.11322

Keeling, C. D., Whorf, T. P., Wahlen, M., & van der Plichtt, J. (1995). Interannual extremes in the rate of rise of atmospheric carbon dioxide since 1980. *Nature*, *375*(6533), 666–670. https://doi.org/10.1038/375666a0

Keeling, R. F., & Scripps Institution of Oceanography. (2023). Scripps CO_2 program, South Pole [Dataset]. Scripps Institution of Oceanography. Retrieved from https://scrippsco2.ucsd.edu/data/atmospheric_co2/spo.html

Keeling, R. F., Piper, S. C., & Heimann, M. (1996). Global and hemispheric CO_2 sinks deduced from changes in atmospheric O_2 concentration. *Nature*, *381*(6579), 218–221. https://doi.org/10.1038/381218a0

Keen, R. A. (1983). Volcanic aerosols and lunar eclipses. *Science*, *222*(4627), 1011–1013. https://doi.org/10.1126/science.222.4627.1011

Kendall, M. G. (1948). Rank correlation methods.

Knorr, W. (2009). Is the airborne fraction of anthropogenic CO_2 emissions increasing? *Geophysical Research Letters*, *36*(21), 1–5. https://doi.org/10.1029/2009GL040613

Lan, X., Tans, P., & Thoning, K. W. (2023). Trends in globally-averaged CO_2 determined from NOAA Global Monitoring Laboratory measurements (version 2023-2012) [Dataset]. NOAA. https://doi.org/10.15138/9N0H-ZH07

Lean, J. L., & Rind, D. H. (2008). How natural and anthropogenic influences alter global and regional surface temperatures: 1889 to 2006. *Geophysical Research Letters*, *35*(18), 1–6. https://doi.org/10.1029/2008GL034864

Le Quéré, C., Raupach, M. R., Canadell, J. G., Marland, G., Bopp, L., Ciais, P., et al. (2009). Trends in the sources and sinks of carbon dioxide. *Nature Geoscience*, *2*(12), 831–836. https://doi.org/10.1038/ngeo689

Lucht, W., Prentice, I. C., Myneni, R. B., Sitch, S., Friedlingstein, P., Cramer, W., et al. (2002). Climatic control of the high-latitude vegetation greening trend and Pinatubo effect. *Science*, *296*(5573), 1687–1689. https://doi.org/10.1126/science.1071828

Malik, A., Brönnimann, S., Stickler, A., Raible, C. C., Muthers, S., Anet, J., et al. (2017). Decadal to multi-decadal scale variability of Indian summer monsoon rainfall in the coupled ocean-atmosphere-chemistry climate model SOCOL-MPIOM. *Climate Dynamics*, *49*(9–10), 3551–3572. https://doi.org/10.1007/s00382-017-3529-9

Mann, H. B. (1945). Nonparametric tests against trend. *Econometrica: Journal of the Econometric Society*, *13*(3), 245–259. https://doi.org/10.2307/1907187

McBride, L. A., Hope, A. P., Canty, T. P., Bennett, B. F., Tribett, W. R., & Salawitch, R. J. (2021). Comparison of CMIP6 historical climate simulations and future projected warming to an empirical model of global climate. *Earth System Dynamics*, *12*(2), 545–579. https://doi.org/10.5194/esd-12-545-2021

Medhaug, I., Stolpe, M. B., Fischer, E. M., & Knutti, R. (2017). Reconciling controversies about the "global warming hiatus.". *Nature*, *545*(7652), 41–47. https://doi.org/10.1038/nature22315

Nicholls, Z., Meinshausen, M., Lewis, J., Corradi, M. R., Dorheim, K., Gasser, T., et al. (2021). Reduced complexity model Intercomparison Project Phase 2: Synthesizing Earth system knowledge for probabilistic climate projections. *Earth's Future*, *9*(6), 1–25. https://doi.org/10.1029/2020EF001900

NOAA/CPC. (2023). Monthly atmospheric & SST indices [Dataset]. NOAA/CPC. Retrieved from https://www.cpc.ncep.noaa.gov/data/indices/

Ogilvie, C. J., & Toohey, M. (2022). CMIP 1850 to 2014 stratospheric extinction coefficients 550nm (Version 3). [Dataset]. University of Saskatchewan ARG GitLab. Retrieved from https://arggit.usask.ca/cj/eva-data-hub/-/tree/main/data

Pan, X., Chin, M., Ichoku, C. M., & Field, R. D. (2018). Connecting Indonesian fires and drought with the type of El Niño and phase of the Indian Ocean Dipole during 1979–2016. *Journal of Geophysical Research: Atmospheres*, *123*(15), 7974–7988. https://doi.org/10.1029/2018JD028402

Pressburger, L., Dorheim, K., Keenan, T. F., McJeon, H., Smith, S. J., & Bond-Lamberty, B. (2023). Quantifying airborne fraction trends and the destination of anthropogenic CO_2 by tracking carbon flows in a simple climate model. *Environmental Research Letters*, *18*(5), 054005. https://doi.org/10.1088/1748-9326/acca35

Pugh, T. A. M., Jones, C. D., Huntingford, C., Burton, C., Arneth, A., Brovkin, V., et al. (2018). A large committed long-term sink of carbon due to vegetation dynamics. *Earth's Future*, *6*(10), 1413–1432. https://doi.org/10.1029/2018EF000935

Raupach, M. R., Canadell, J. G., & Le Quéré, C. (2008). Anthropogenic and biophysical contributions to increasing atmospheric CO_2 growth rate and airborne fraction. *Biogeosciences*, *5*(6), 1601–1613. https://doi.org/10.5194/bg-5-1601-2008

Raupach, M. R., Gloor, M., Sarmiento, J. L., Canadell, J. G., Frölicher, T. L., Gasser, T., et al. (2014). The declining uptake rate of atmospheric CO_2 by land and ocean sinks. *Biogeosciences*, *11*(13), 3453–3475. https://doi.org/10.5194/bg-11-3453-2014

Revelle, R., & Suess, H. E. (1957). Carbon dioxide exchange between atmosphere and ocean and the question of an increase of atmospheric CO_2 during the Past Decades. *Tellus*, *9*(1), 18–27. https://doi.org/10.3402/tellusa.v9i1.9075

Reynolds, R. W., Rayner, N. A., Smith, T. M., Stokes, D. C., & Wang, W. (2002). An improved in situ and satellite SST analysis for climate. *Journal of Climate*, *15*(13), 1609–1625. https://doi.org/10.1175/1520-0442(2002)015<1609:AIISAS>2.0.CO;2

Ruddiman, W. F., He, F., Vavrus, S. J., & Kutzbach, J. E. (2020). The early anthropogenic hypothesis: A review. *Quaternary Science Reviews*, *240*, 106386. https://doi.org/10.1016/j.quascirev.2020.106386

Sasaki, W., Doi, T., Richards, K. J., & Masumoto, Y. (2015). The influence of ENSO on the equatorial Atlantic precipitation through the Walker circulation in a CGCM. *Climate Dynamics*, *44*(1–2), 191–202. https://doi.org/10.1007/s00382-014-2133-5

Sato, M., Hansen, J. E., Lacis, D., & Pollack, J. B. (2016). Stratospheric aerosol optical thickness [Dataset]. NASA. Retrieved from https://data.giss.nasa.gov/modelforce/strataer/

Sato, M., Hansen, J. E., McCormick, M. P., & Pollack, J. B. (1993). Stratospheric aerosol optical depths, 1850-1990. *Journal of Geophysical Research*, *98*(D12), 22987–22994. https://doi.org/10.1029/93JD02553

Sellar, A. A., Walton, J., Jones, C. G., Wood, R., Abraham, N. L., Andrejczuk, M., et al. (2020). Implementation of U.K. Earth System Models for CMIP6. *Journal of Advances in Modeling Earth Systems*, *12*(4), 1–27. https://doi.org/10.1029/2019MS001946

Sellers, P. J., Schimel, D. S., Moore, B., III., Liu, J., & Eldering, A. (2018). Observing carbon cycle-climate feedbacks from space. *Proceedings of the National Academy of Sciences*, *115*(31), 7860–7868. https://doi.org/10.1073/pnas.1716613115

Sen, P. K. (1968). Estimates of the regression coefficient based on Kendall's tau. *Journal of the American Statistical Association*, *63*(324), 1379–1389. https://doi.org/10.1080/01621459.1968.10480934

Siegenthaler, U., & Oeschger, H. (1987). Biospheric CO_2 emissions during the past 200 years reconstructed by deconvolution of ice core data. *Tellus*, *39 B*(1–2), 140–154. https://doi.org/10.3402/tellusb.v39i1-2.15331

Smith, N. G., & Dukes, J. S. (2017). Short-term acclimation to warmer temperatures accelerates leaf carbon exchange processes across plant types. *Global Change Biology*, *23*(11), 4840–4853. https://doi.org/10.1111/gcb.13735

Tans, P., & NOAA/GML. (2023). Trends in atmospheric carbon dioxide at Mauna Loa, Hawaii [Dataset]. NOAA/GML. Retrieved from https://gml.noaa.gov/ccgg/trends/data.html

Teckentrup, L., De Kauwe, M. G., Pitman, A. J., & Smith, B. (2021). Examining the sensitivity of the terrestrial carbon cycle to the expression of El Niño. *Biogeosciences*, *18*(6), 2181–2203. https://doi.org/10.5194/bg-2020-299

Thomason, L. W., Ernest, N., Millán, L., Rieger, L., Bourassa, A., Vernier, J.-P., et al. (2018). A global space-based stratospheric aerosol climatology: 1979–2016. *Earth System Science Data*, *10*(1), 469–492. https://doi.org/10.5194/essd-10-469-2018

Thomason, L. W., Ernest, N., Millán, L., Rieger, L., Bourassa, A., Vernier, J.-P., et al. (2022). Global satellite-based stratospheric aerosol climatology (GloSSAC) (version 2.2) [Dataset]. NASA. https://opendap.larc.nasa.gov/opendap/GloSSAC/GloSSAC_2.2/contents.html

Toohey, M., Stevens, B., Schmidt, H., & Timmreck, C. (2016). Easy Volcanic Aerosol (EVA v1.0): An idealized forcing generator for climate simulations. *Geoscientific Model Development*, *9*(11), 4049–4070. https://doi.org/10.5194/gmd-9-4049-2016

van der Werf, G. R., Dempewolf, J., Trigg, S. N., Randerson, J. T., Kasibhatla, P. S., Giglio, L., et al. (2008). Climate regulation of fire emissions and deforestation in equatorial Asia. *Proceedings of the National Academy of Sciences of the United States of America*, *105*(51), 20350–20355. https://doi.org/10.1073/pnas.0803375105

van Marle, M. J. E., van Wees, D., Houghton, R. A., Field, R. D., Verbesselt, J., & van der Werf, G. R. (2022). New land-use-change emissions indicate a declining CO_2 airborne fraction. *Nature*, *603*(7901), 450–454. https://doi.org/10.1038/s41586-021-04376-4

van Marle, M. J. E., van Wees, D., Houghton, R. A., Field, R. D., Verbesselt, J., & van der Werf, G. R. (2023). Retraction note: New land-use-change emissions indicate a declining CO_2 airborne fraction. *Nature*, *622*(7981), 202. https://doi.org/10.1038/s41586-023-06605-4

Wang, J., Zeng, N., Wang, M., Jiang, F., Chen, J., Friedlingstein, P., et al. (2018). Contrasting interannual atmospheric CO_2 variabilities and their terrestrial mechanisms for two types of El Niños. *Atmospheric Chemistry and Physics*, *18*(14), 10333–10345. https://doi.org/10.5194/acp-18-10333-2018

Xi, F., Davis, S. J., Ciais, P., Crawford-Brown, D., Guan, D., Pade, C., et al. (2016). Substantial global carbon uptake by cement carbonation. *Nature Geoscience*, *9*(12), 880–883. https://doi.org/10.1038/ngeo2840

Zhang, Y., Dannenberg, M. P., Hwang, T., & Song, C. (2019). El Niño-Southern Oscillation-induced variability of terrestrial gross primary production during the satellite era. *Journal of Geophysical Research: Biogeosciences*, *124*(8), 2419–2431. https://doi.org/10.1029/2019JG005117

Zhao, M., & Running, S. W. (2010). Drought-induced reduction in global. *Science*, *329*(5994), 940–943. https://doi.org/10.1126/science.1192666